

# One-dimensional many-body entangled open quantum systems with tensor network methods

Daniel Jaschke,<sup>1</sup> Simone Montangero,<sup>2,3,4</sup> and Lincoln D. Carr<sup>1</sup>

<sup>1</sup>*Department of Physics, Colorado School of Mines, Golden, Colorado 80401, USA*

<sup>2</sup>*Institute for Complex Quantum systems and Center for Integrated Quantum Science and Technologies, Universität Ulm, D-89069 Ulm, Germany*

<sup>3</sup>*Theoretische Physik, Universität des Saarlandes, D-66123 Saarbrücken, Germany*

<sup>4</sup>*Dipartimento di Fisica e Astronomia, Università degli Studi di Padova, I-35131 Italy*

We present a collection of methods to simulate entangled dynamics of open quantum systems governed by the Lindblad master equation with tensor network methods. Tensor network methods using matrix product states have been proven very useful to simulate many-body quantum systems and have driven many innovations in research. Since the matrix product state design is tailored for closed one-dimensional systems governed by the Schrödinger equation, the next step for many-body quantum dynamics is the simulation of one-dimensional open quantum systems. We review the three dominant approaches to the simulation of open quantum systems via the Lindblad master equation: quantum trajectories, matrix product density operators, and locally purified tensor networks. Selected examples guide possible applications of the methods and serve moreover as a benchmark between the techniques. These examples include the finite temperature states of the transverse quantum Ising model, the dynamics of an exciton traveling under the influence of spontaneous emission and dephasing, and a double-well potential simulated with the Bose-Hubbard model including dephasing. We analyze which approach is favorable leading to the conclusion that a complete set of all three methods is most beneficial, pushing the limits of different scenarios. The convergence studies using analytical results for macroscopic variables and exact diagonalization methods as comparison, show, for example, that matrix product density operators are favorable for the exciton problem in our study. All three methods access the same library, i.e., the software package *Open Source Matrix Product States*, allowing us to have a meaningful comparison between the different approaches based on the selected examples. For example, tensor operations are accessed from the same subroutines and with the same optimization eliminating one possible bias in a comparison of such numerical methods.

## CONTENTS

I. Introduction	2
II. Theoretical Approaches to the Simulation of Open Quantum Systems	3
III. Tensor Networks Simulations of the Lindblad Master Equation	4
A. Matrix Product Density Operators	4
B. Quantum Trajectories	10
C. Locally Purified Tensor Networks	12
IV. Simulation Setup and Convergence	13
A. Finite-T states in the Ising model (MPDO and LPTN)	14
B. Local Lindblad operators without symmetry (QT, MPDO, and LTPN)	15
C. Local Lindblad operators with symmetry (QT and MPDO)	18
V. Conclusions	19
Acknowledgments	20
References	20
A. Non-Local Lindblad operators with symmetry (MPDO)	23
B. Bond dimension infinite-T Bose-Hubbard state	24

## I. INTRODUCTION

The study of the combination of many-body quantum systems and open systems is one of the critical pieces *needed* to develop powerful quantum simulators and quantum computers. While the many-body part is strictly necessary to scale these systems to sizes useful for applications, open quantum systems help one to understand the effects of decoherence and, therefore, the lifetime of the actual system. Further questions are the analysis of steady states and the transient dynamics approaching them. Reservoir engineering has the purpose of preparing the system in a defined state; this state is equal to the steady state and, therefore, protected from decoherence. The process of thermalization is another example for open quantum system research. The open system implementations in our *Open Source Matrix Product States* (OSMPS) package combine two popular approaches: tensor networks for many-body simulations and the Lindblad master equation as a default approach for Markovian open quantum systems.

The Lindblad master equation [1–3] is one common approach to open quantum systems [4–7], although its limitations are well-known. The benefit of this approach is the conservation of the properties of the density matrix, i.e., norm and positivity. The assumptions during the derivation, e.g., the Born-Markov and secular approximation, limit the use of the Lindblad master equation to quantum systems weakly coupled to large reservoirs. Other approaches to open quantum systems are for example hierarchical equations of motions [8, 9] or various techniques for non-Markovian open quantum systems [10], but a versatile implementation of the Lindblad equation is the first step towards the implementation of a tensor network suite to study open quantum systems.

The history of tensor networks for quantum mechanics reaches back to the density matrix renormalization group (DMRG) [11–13], then recasted into the matrix product state (MPS) language [14–16]; recent papers highlight the equivalence between the two approaches [17]. Based on the original MPS idea, many different tensor networks have been derived ranging from tree-tensor networks (TTN) [18] over the multi-scale entanglement renormalization ansatz (MERA) [19] to projected entangled pair states (PEPS) [20], where the latter is designed for two-dimensional systems; TTN and MERA can solve both one-dimensional systems and generalizations to higher dimension. Approaches such as PEPS can also be generalized to simulate open system in two dimensions, as recently shown in [21]. We focus in this work on one-dimensional systems in an MPS-like chain structure. Tensor networks are very-well suited for this kind of low-dimensional many-body system, where the area law describing the scaling of the entanglement is the most favorable [22]. We concentrate on tensor networks for the time evolution of open systems and a background in MPS techniques is assumed. We emphasize that the steady state of an open quantum system can be calculated variationally [23–25], which is not included in this work. The point of this paper is the side-by-side discussion of three different approaches relating the technical implementation and their implications for the convergence of actual simulations. The first of the three approaches are quantum trajectories (QT) [26–30] providing a statistical approach to the Lindblad master equation. In contrast, both matrix product density operators (MPDOs) [31, 32] and locally purified tensor networks (LPTNs) [33] simulate the complete density matrix. The latter two approaches can also simulate thermal states, which are otherwise only accessible through METTS [34] or after building a sufficient number of eigenstates. Both MPDO and LPTN representations have their limitations as discussed in References [35–37]. Very briefly, the arguments against each approach are that MPDOs do not conserve positivity and the corresponding check is an NP-hard problem. In contrast, there are states which have a representation in terms of MPDOs and maintain translational invariance, while LPTNs leak a similar representation for this set of states. We point out that there are previous comparisons between two of the methods [38].

Possible applications arise in the fast-evolving fields of quantum simulators and quantum computing experiments. Rydberg systems are one promising platform for quantum simulators, and reference [39] outlines their possible applications within the framework of the Lindblad master equation. The Lindblad operators described therein are quasi-local, meaning acting on a neighborhood of sites. The treatment of superconducting qubits coupled to phonon modes is another architecture [40], allowing one to couple the superconducting qubit to other degrees of freedom in the systems. The Lindblad equation was used in this context to simulate the lifetime of the phonon modes [41]. Trapped ions system are considered to be quantum simulators for open systems themselves as pointed out in references [42, 43]. Although the primary focus is on simulating open quantum systems according to Kraus operators, the application of numerical simulations to this scenario seems very fruitful to us given the connection between Lindblad equation and Kraus operators [44]. The review in [45] highlights the quantum simulator applications of Rydberg systems and trapped ions. Moreover, it lists examples for ultracold atoms systems in an open system context. The atomic, molecular, and optical (AMO) platforms provide another set of problems to be studied. Atomic bosons can heat due to the interaction with the optical lattice [46], and molecules have even more degrees of freedom [47] to be used within open quantum systems. The different internal degrees of freedom, i.e., rovibrational and motional degrees of freedom, can be used for encoding individual reservoirs for each molecule; one degree of freedom acts as a system, while another degree of freedom acts as a reservoir for the first [48]. This incomplete list shows the possible application of open quantum systems in the quantum simulator context. We argue that the consideration of system-environment effects will be an even more intensive focus of future research as decoherence times of experiments increase and errors decrease.

The outline of the paper is as follows. Section II is a very brief review of methods used to simulate open quantum systems with tensor network methods. Section III provides the actual details of the implementation in the OSMPS package. We follow the structure of earlier work [49] connecting the different time evolution methods to the open system. The setup of the simulations

and their convergence is discussed in Sec. IV, where this section contains the showcases of applications. The finite temperature states are the first example in Sec. IV A, where the quantum Ising model is one possibility to describe many two-level quantum systems. Section IV B turns to the transport of an exciton, which travels under the influence of the interaction with an environment. The last example considers a double-well potential governed by the Bose-Hubbard model, where the oscillation between left and right well are damped out in the open quantum system, see Sec. IV C. We conclude in Sec. V. Appendix A provides additional aspects of non-local Lindblad operator for the example of a dissipative state preparation; Appendix B provides technical details on the bond dimension of finite temperature states with symmetries.

## II. THEORETICAL APPROACHES TO THE SIMULATION OF OPEN QUANTUM SYSTEMS

Before going into details of the numerical setup for the simulation of the Lindblad master equation, it is worthwhile to keep in mind the existing alternative approaches for the simulation of open quantum systems. Amongst all the different techniques which have been outlined for open quantum systems are stochastic methods [50], Redfield master equations [4], or solving the full system. Some of these methods are within the reach of tensor network methods, e.g., the Redfield master equation. Others, i.e., the simulation of the full system, can already be achieved with MPS methods as long as system plus environment together are not too big. The Lindblad master equation is the first choice among above list as it conserves norm, Hermiticity, and positivity of the state. OSMPS uses the Lindblad equation

$$\dot{\rho} = \frac{i}{\hbar}[\rho, H] + \sum_{\nu} L_{\nu} \rho L_{\nu}^{\dagger} - \frac{1}{2}\{L_{\nu}^{\dagger} L_{\nu}, \rho\}, \quad (1)$$

which describes the evolution of the density matrix  $\rho$  under the Hamiltonian  $H$  and a set of Lindblad operators  $L_{\nu}$ . Thereafter,  $\hbar$  is set to one. As we are treating many-body systems, the index  $\nu$  can be a combined index running itself over the different Lindblad operators  $\mu$  and different sites  $k$  in the system, i.e.,  $\nu = (\mu, k)$ . The Lindblad equation includes the approximations explained as follows. Ideally, given unlimited resources, we would simulate the Schrödinger equation for the system  $S$  of interest and its environment  $E$

$$\frac{\partial}{\partial t} |\psi_{S+E}\rangle = -\frac{i}{\hbar} H_{S+E}(t) |\psi_{S+E}\rangle. \quad (2)$$

Considering that the environment can be enormous and the Hilbert space grows exponentially with system size, we apply the following three approximations to Eq. (2) to obtain the Lindblad equation. (i) System and environment are in a product state at  $t = 0$  and stay in a product state over the time evolution, i.e.,  $\rho_{S+R}(t) = \rho_S(t) \otimes \rho_E$ . Correlations decay fast if the reservoir is large and the reservoir remains unperturbed by the interaction with the system. This assumption settles the timescales between the environment  $\tau_E$  and the system  $\tau_S$ :  $\tau_E \ll \tau_S$ . (ii) Furthermore, the timescale of the system holds  $\tau_S \ll \tau_{S,\text{eq}}$ ; the equilibration time of the system  $\tau_{S,\text{eq}}$  is longer than the time step. (iii) We truncate fast oscillating terms similar to the rotating wave approximation when considering transitions of different frequencies in the system, where their difference sets the timescale. These approximations are formally described in terms of the Born-Markov approximation, i.e., (i) and (ii), and the secular approximation, see (iii).

In order to simulate a system according to the Lindblad master equation, we distinguish two paths. QTs evolve pure states sampling over a variety of trajectories. This approach is motivated by the fact that in an experimental setup every measurement projects the density matrix into a pure state; we assume that the measurement outcomes are non-degenerate for each state for simplicity. The QT approach models the probability for the projection into a specific state. Therefore, a single simulation only reflects one possible outcome of an experiment. To obtain the outcome for Eq. (1), sampling over different trajectories is necessary. One advantage of this method is that we use pure states and there is no significant increase in the computational scaling with respect to an MPS simulation for each trajectory. The local dimension of the MPS used in each QT is the same as for the MPS in a closed system. Furthermore, any MPS can be used as initial state without increasing the bond dimension prior to the time evolution. During the time evolution, we rely on the capabilities of the MPS compression scheme to reduce entanglement, which is obsolete after a quantum jump. The additional steps for choosing the Lindblad operator to be applied to the MPS are not significant. The computational scaling of the open quantum system is reflected in the number of trajectories. The different trajectories can be easily parallelized across different cores with MPI (Message Passing Interface).

On the other hand,  $\rho$  can be directly simulated, e.g, mapping the density matrix  $\rho$  to a superket vector  $|\rho\rangle\rangle$  [31, 32] resulting in a Schrödinger-like equation. The superket  $|\rho\rangle\rangle$  is constructed by building a vector out of all entries in the density matrix  $\rho$ . The governing equation is then

$$\frac{\partial}{\partial t} |\rho\rangle\rangle = \mathcal{L}(t) |\rho\rangle\rangle, \quad (3)$$

where the non-Hermitian Liouville operator  $\mathcal{L}(t)$  corresponds to the Hamiltonian and is defined as:

$$\begin{aligned} \mathcal{L}(t) = & -\frac{i}{\hbar} H(t) \otimes \mathbb{I} + \frac{i}{\hbar} \mathbb{I} \otimes H^T(t) \\ & + \sum_{\nu} L_{\nu} \otimes (L_{\nu}^{\dagger})^T - \frac{1}{2} \left( L_{\nu}^{\dagger} L_{\nu} \otimes \mathbb{I} + \mathbb{I} \otimes (L_{\nu}^{\dagger} L_{\nu})^T \right). \end{aligned} \quad (4)$$

Overall, this approach allows us to simulate systems replacing the Hamiltonian with  $\mathcal{L}$  at the cost of increased local dimension. If the total dimension of the closed system is  $D$ , the dimension of the problem in Liouville space is  $D^2$ .

Finally, we can evolve the purification of  $\rho$  denoted with  $X$  [33]. Since the density matrix is by definition positive, we can decompose it into

$$\rho = X X^{\dagger}. \quad (5)$$

For example, a pure state  $|\psi\rangle$  is equal to its purification  $X = |\psi\rangle$ . To preserve the structure of the complex conjugate pair, we use instead of Eq. (1) the more general Kraus operators representing a completely positive trace preserving map (CPT map):

$$\rho(t + dt) = \sum_{\nu'} K_{\nu'} \rho(t) K_{\nu'}^{\dagger} \quad (6)$$

$K_{\nu'}$  are called Kraus operators. There is a connection to derive the Kraus operators via Choi's theorem from the Lindblad equation [51], or we approximate the Kraus operators in first order in  $dt$  and truncating higher order terms of  $dt$  when expanding  $\rho(t + dt) \approx \rho(t) + dt \dot{\rho}(t)$  with  $\dot{\rho}(t)$  as defined in the Lindblad master equation (1) [44].

The MPS algorithms profit from considerable speed-ups when symmetries are present in the system and encoded to the tensor network. We distinguish between Abelian symmetries, considered in the following, and non-Abelian symmetries. Abelian groups are preferable from the perspective of an implementation as operations commute and keeping track of quantum numbers reduces to a simple group operations; in contrast, non-Abelian groups have to use the Clebsch-Gordan coefficients. We can use symmetries in the Schrödinger equation when the commutation of some operator  $G$  commutes with the Hamiltonian,  $[H, G] = 0$ , and has a definition in terms of the local Hilbert spaces. For example, the Bose-Hubbard model conserves the number of particles and  $N = \sum_k n_k$  commutes with the Bose-Hubbard Hamiltonian, see later on in Eq. (A1). We can also use the Abelian symmetry in the Liouville equation if the Lindblad operators do not violate the symmetry,

$$[\mathcal{L}, G \otimes \mathbb{I} + \mathbb{I} \otimes G^T] = 0. \quad (7)$$

Thus, we cannot add loss of particles with an annihilation operator as a Lindblad operator in a number-conserving simulations: the Lindblad operator violates the symmetry.

This brief overview enables us to take a closer look at the different evolution methods in Sec. III.

### III. TENSOR NETWORKS SIMULATIONS OF THE LINDBLAD MASTER EQUATION

This section covers the technical aspects of all three approaches to open quantum systems. We start with the simulation of the Lindblad master equation in terms of MPDOs [31, 32] and describe in detail the issues raised by a non-Hermitian operator. The quantum trajectories [26, 27, 52] share the non-Hermitian operator with the MPDOs, and we explain quantum trajectories in the following section. Finally, we discuss the third approach using LPTNs [33]. Once we have covered these aspects, we turn to the convergence of the different approaches. Readers aware of the technical details or solely interested in the practical application of the methods may, therefore, skip this section and to straight to Sec. IV.

#### A. Matrix Product Density Operators

The formulation of MPDOs heavily relies on the Liouville operator and superket notation in Eq. (4) and the similarity to the Schrödinger equation. The first steps into the MPDOs implementation inside OSMPS describe the notations of the superket  $|\rho\rangle\rangle$  and we first introduce the static aspect of MPDOs, i.e., their ability to calculate thermal states. Then, we move toward matrix product operators (MPOs) [53, 54] of the Liouville operator. Knowing these two principal objects, i.e., the superket and the MPO, we move forward to the time-evolution methods using the MPO, i.e., Krylov, local Runge-Kutta (LRK) [55], and the time-dependent variational principle (TDVP) [56]. Finally, we fill in the description of the Krylov time-evolving block decimation (KTEBD) and the well-established time-evolving block decimation (TEBD) [14] algorithm and its modifications for the evolution of the Lindblad master equation. In fact, the time evolution methods for the quantum trajectories revisit many issues already discussed here as both methods deal with a non-Hermitian propagator.

### 1. Construction of Matrix Product Density Operator states

We limit ourselves to the construction of two classes of initial states for the time evolution. On the one hand, we convert MPS states to MPDOs. Suitable MPS states include product states, ground states, low-lying excited states, and pure states obtained via unitary time evolution. On the other hand, we would like to have finite temperature states via an imaginary time evolution of MPDOs. Therefore, the infinite temperature state has to be given as an initial state for the imaginary time evolution as it serves as a starting point for cooling. This procedure is explained in Sec. III A 2. With the knowledge of the infinite temperature state which is a mixed product state, the construction for product states of any other type can be derived.

Figure 1 describes the transformation of an MPS into an MPDO. If the tensor  $A_{\alpha,i,\beta}^{[k]}$  represents the site  $k$  in the MPS, we add an auxiliary link of dimension one and obtain  $A_{\alpha,i,\kappa,\beta}^{[k]}$ . We contract this tensor with its complex conjugate tensor  $(A_{\alpha',i',\kappa,\beta'}^{[k]})^*$  over  $\kappa$  leading to the MPDO representation  $B_{(\alpha,\alpha'),(i,i'),(\beta,\beta')}^{[k]}$ . The contraction over the auxiliary index corresponds to the outer product  $|\psi\rangle\langle\psi|$ , taken locally on site  $k$ . Thus, the usage of an outer product is an alternative to the auxiliary index. The indices in parentheses represent fused indices; therefore, the new tensor is again of rank 3. The fusion of two indices produces a new index using a Cartesian product to map the elements, e.g.,  $\alpha, \alpha' \rightarrow (\alpha, \alpha') = \alpha''$ . The dimension of the new index  $\alpha''$  is the product of the dimension of the two original indices  $\alpha$  and  $\alpha'$ . We notice the increase in the dimension of links: for a tensor with bond dimensions  $(\chi, d, \chi)$  in the MPS, the new bond dimensions in the MPDO are  $(\chi^2, d^2, \chi^2)$ . The number of sub-tensors for a symmetric tensor network also increases. If we have  $n$  sub-tensors in an MPS site, the MPDO representation of the site has  $n^2$  sub-tensors.

The infinite temperature state  $\rho_\infty$  is straightforward to implement in an MPDO without symmetries but has some subtleties when symmetries are used. The density matrix  $\rho_\infty$  is the identity matrix normalized to trace one. If we do not have symmetries, the global identity is a product of local identities  $\rho_\infty \propto \bigotimes_{k=1}^L 1_k$ . Thus, the bond dimension between sites in the MPDO is  $\chi = 1$ , and the tensors are  $B_{\alpha,(i,i'),\beta} = \delta_{ii'}$ . In contrast, the product of local identity for a symmetric MPDO contains states in all possible symmetry sectors and does not lead to  $\rho_\infty$  for a specific sector. Instead, we construct the state  $\rho_\infty$  representing the Gibbs distribution at infinite temperature from symmetric sub-tensors on each site  $k$  filled with

$$B_{\alpha,(i,i'),\beta}^{[k]}((q_1, q'_1), (q_2, q'_2), (q_3, q'_3)) = \delta_{ii'} \delta_{q_1 q'_1} \delta_{q_2 q'_2}. \quad (8)$$

The incoming quantum number from the left must be chosen in such a way that is possible to obtain it with the local Hilbert spaces on the left. The outgoing quantum number  $q_3 = q_1 + q_2$  must allow us to have the sector specified:  $q_3^{[k=L]}$  on the last site must match the global sector exactly. We illustrate these choices with the Bose-Hubbard model with a maximum filling of 3, i.e., local dimension  $d = 4$ . Further, we specify the system size  $L = 5$  and unit filling.  $q_1^{[k=2]} \in \{0, 1, 2, 3\}$  for the second site  $k = 2$ ,  $q_1^{[l=2]} = 4$  cannot be achieved from a single site on the left. Similar, for the fourth site  $k = 4$ ,  $q_3^{[k=4]} \in \{2, 3, 4, 5\}$ . Any lower filling cannot reach unit filling with a single site on the right. Higher  $q_3^{[k=4]}$  are already above unit filling and do not match the symmetry sector. In conclusion, the symmetric  $\rho_\infty$  has already a bond dimension  $\chi > 1$  from the beginning and can contain a large number of sub-tensors. For example, the bond dimension of the Bose-Hubbard model on  $L$  sites with maximal filling  $d - 1$  for each site has an upper bound for the bond dimension of  $d(N - d + 2)$  distributed on the block-diagonal structure. We present a detailed calculation in Appendix B. A generalization to more complicated symmetries is possible, but a generalized equation for the maximal bond dimension of any model and symmetry is difficult to obtain.

### 2. Imaginary time evolution for finite-T states

The finite temperature (finite-T) states are based on the Gibbs distribution defined as  $\rho(T) = \exp(-H/(k_B T))/\mathcal{N}$  with  $\mathcal{N} = \text{Tr}[\exp(-H/(k_B T))]$  and  $k_B = 1$  the Boltzmann constant and have been pointed out as a feature of MPDOs from their definition on [31, 32]. From the Gibbs distribution, we rewrite the unnormalized state as

$$\begin{aligned} e^{-H/(k_B T)} &= e^{-H/(2k_B T)} \mathbb{I} e^{-H/(2k_B T)} \\ &\propto e^{-H/(2k_B T)} \rho_\infty e^{-H/(2k_B T)} \\ &= e^{\frac{1}{2k_B T} (-H \otimes \mathbb{I} - \mathbb{I} \otimes H^T)} |\rho_\infty\rangle\rangle, \end{aligned} \quad (9)$$

which corresponds to an imaginary time evolution similar to the ground state algorithm of an MPS. The operator in Liouville space is Hermitian. In detail, we enable the TEBD algorithms for imaginary time evolution. The definition of the initial state  $|\rho_\infty\rangle\rangle$  was discussed in the previous Sec. III A 1 as an example of how to construct initial states represented as an MPDO.

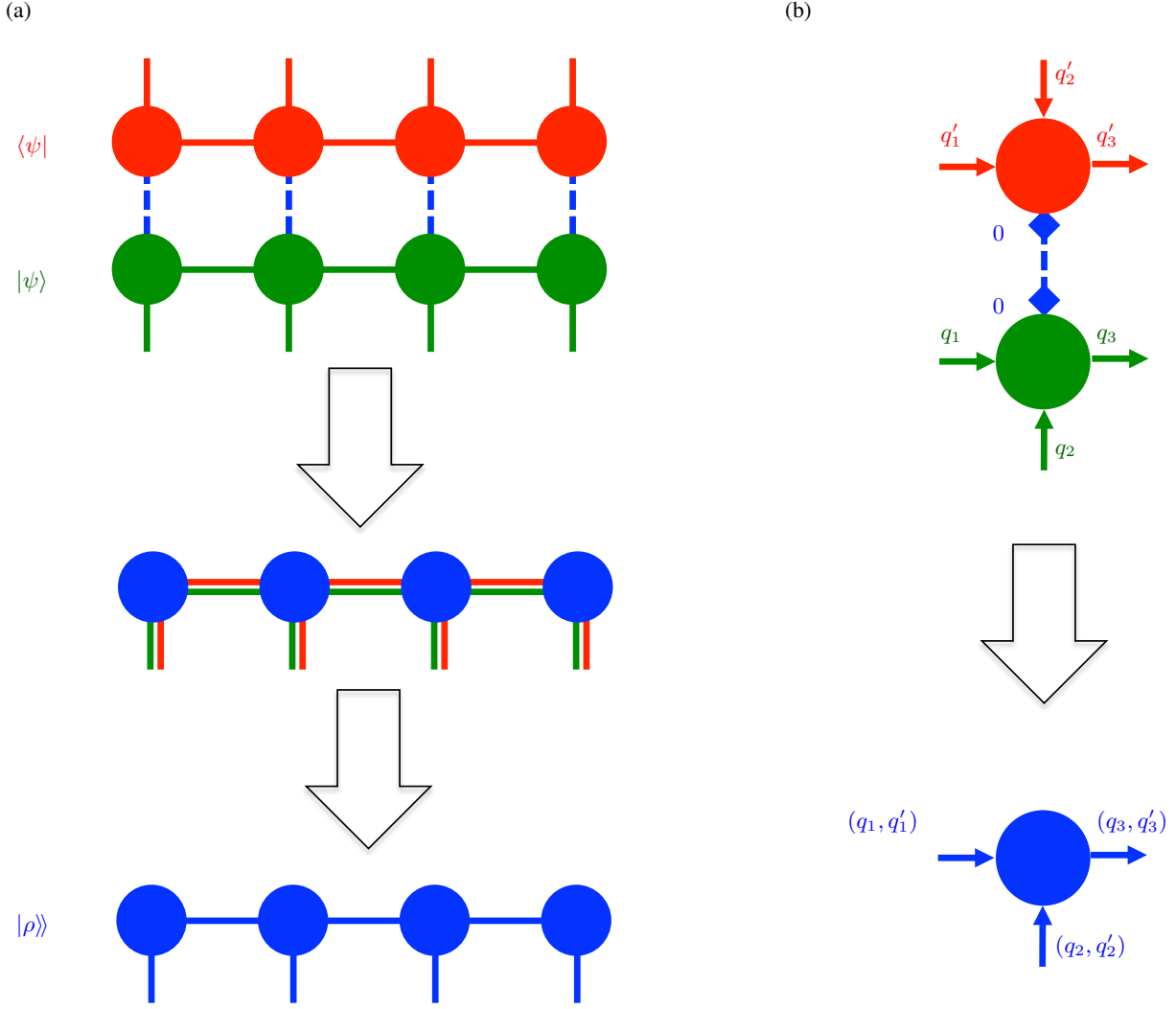


Figure 1. *MPDO from MPS state.* (a) In an MPS without symmetries, each site tensor is contracted over a one-dimensional auxiliary link with its complex conjugated counterpart. The corresponding links are fused. (b) The auxiliary tensor contracted over in an MPS with symmetries is labeled with a dummy quantum number 0. We get all combination of sub-tensors. In addition to merging the links of the sub-tensors, the quantum numbers are combined.

### 3. Matrix Product Operators in Liouville space

For the simulation of the Lindblad master equation with matrix MPO techniques, we transform Eq. (1) into the Liouville space. This transformation allows us to represent the density matrix as vector  $|\rho\rangle\rangle$  and use MPS techniques developed for pure states on an enlarged local space. The local dimension  $d$  for pure states  $|\psi\rangle$  translates into a local dimension  $d_{\mathcal{L}} = d^2$  for the simulation of  $|\rho\rangle\rangle$ . In recent work [49], we presented the evolution techniques in the OSMPS package for pure states based on formulating the Hamiltonian  $H$  of the system as an MPO. We can reuse all evolution techniques for MPDOs once we can formulate  $\mathcal{L}$  as an MPO. We restrict the Hamiltonian to local terms and bond terms, i.e., nearest neighbor interactions, to explain the procedure. But the methods are generalized to any rule set present in OSMPS for the Liouville space. For the MPS evolution, we know that the bond dimension of the MPO for  $n_{\text{site}}$  local terms and  $n_{\text{bond}}$  nearest neighbor terms is  $\chi_{\text{MPO}} = 2 + n_{\text{bond}}$ . We explain how to build the MPO matrices along the quantum Ising model with the Hamiltonian

$$H_{\text{QI}} = -J \sum_{j=1}^{L-1} \sigma_j^z \sigma_{j+1}^z - g \sum_{j=1}^L \sigma_j^x, \quad (10)$$

where  $\sigma_j^x$  and  $\sigma_j^z$  are the Pauli matrices acting on site  $j$ . The interaction strength between neighboring spins is  $J$ , the coupling to the external field is  $g$ , and the system size is  $L$ . The MPO operator-valued matrix in the bulk of the system for the Hamiltonian

$H_{\text{QI}}$  is

$$M_H = \begin{pmatrix} \mathbb{I} & 0 & 0 \\ \sigma^z & 0 & 0 \\ -g\sigma^x & -J\sigma^z & \mathbb{I} \end{pmatrix}, \quad (11)$$

where the two of the four dimensions of the rank 4 MPO tensor are encoded into the row and columns of this matrix. These two indices are contracted with left and right neighboring MPO-matrices and the number of rows/columns is the bond dimension of the MPO. The first (last) MPO is an operator-valued row (column) vector. The remaining two dimensions are the dimensions of the matrix for each entry. In this notation, 0 is to be understood as a  $d \times d$  matrix of zeros. A convenient implementation uses operator-valued sparse matrices instead of building the full rank 4 tensor with a large fraction of zeros [54]. We transform this MPO to the Liouville space according to Eq. (3); the relevant terms are the Hamiltonian terms  $H \otimes \mathbb{I} - \mathbb{I} \otimes H^T$ . We reorder the subspaces such that the terms for each site are collected. The two links for the Hilbert space of each site have been fused previously. Thus, the new operator-valued entries have a dimension of  $d^2 \times d^2$ . This transformation increases the MPO bond dimension to  $\chi_{\text{MPO}, \mathcal{L}} = 2 + 2n_{\text{bond}}$ :

$$M_{\mathcal{L}} = \begin{pmatrix} \mathbb{I} & 0 & 0 & 0 \\ \sigma^z \otimes \mathbb{I} & 0 & 0 & 0 \\ \mathbb{I} \otimes (\sigma^z)^T & 0 & 0 & 0 \\ -g\sigma^x \otimes \mathbb{I} - \mathbb{I} \otimes -g(\sigma^x)^T & -J\sigma^z \otimes 1 & -(\mathbb{I} \otimes -J(\sigma^z)^T) & \mathbb{I} \end{pmatrix}. \quad (12)$$

Here in the construction of  $M_{\mathcal{L}}$ , we assume that the  $\mathcal{L}$  is multiplied with the usual  $(-idt)$  in the evolution. The different signs in front of  $H \otimes \mathbb{I}$  and  $\mathbb{I} \otimes H^T$  are considered together with the coupling constant of the Hamiltonian term and are not double-counted. So far, this step allows us to evolve a closed initially pure or mixed system. To include local Lindblad operators  $L_\mu$  acting on each site as part of the dissipative part of the evolution, we add the following matrix based on Eq. (3) to the previous result in Eq. (12), which contains the Hamiltonian part of the evolution in Liouville space:

$$M_{\mathcal{L}} = \begin{pmatrix} 0 & 0 & 0 & 0 \\ 0 & 0 & 0 & 0 \\ 0 & 0 & 0 & 0 \\ i\gamma (L_\mu \otimes L_\mu^* - \frac{1}{2} L_\mu^\dagger L_\mu \otimes \mathbb{I} - \frac{1}{2} \mathbb{I} \otimes L_\mu^T L_\mu^*) & 0 & 0 & 0 \end{pmatrix}. \quad (13)$$

The imaginary unit takes into account the multiplication of  $(-idt)$  leaving only  $dt$  after the construction of the argument for the exponential. Thus, the local Lindblad operators do not increase the bond dimension of the MPO. We implement another type of Lindblad operator similar to a Hamiltonian many-body string term, i.e., the many-body string Lindblad operator

$$L_k(r) = L_k \otimes L_{k+1} \otimes \cdots \otimes L_{k+r-1}. \quad (14)$$

The MPO bond dimension for a many-body string Hamiltonian term is  $r - 1$  for the Hamiltonian, and  $2(r - 1)$  for the Liouville operator. The many-body string Lindblad term has a bond dimension of  $3(r - 1)$ . In detail, we implement three terms with bond dimension  $(r - 1)$ , which are the three different terms in the dissipative part

$$L_k \otimes \cdots \otimes L_{k+r-1} \rho L_k^\dagger \otimes \cdots \otimes L_{k+r-1}^\dagger, \quad (15a)$$

$$-\frac{1}{2} L_k^\dagger L_k \otimes \cdots \otimes L_{k+r-1}^\dagger L_{k+r-1} \rho, \quad (15b)$$

$$-\frac{1}{2} \rho L_k^\dagger L_k \otimes \cdots \otimes L_{k+r-1}^\dagger L_{k+r-1}. \quad (15c)$$

The tripling of the bond dimension for a multi-site Lindblad rule equivalent to a Hamiltonian rule holds in general. Equation (15a) represents  $L\rho L^\dagger$  in the Lindblad equation, see Eq. (1). The other two terms, i.e., Eqs. (15b) and (15c), build the anti-commutator. The setup of  $\mathcal{L}$  as an MPO is the primary step to use the evolution methods. Nonetheless, the MPS methods cannot be used blindly since  $\mathcal{L}$  does not necessarily maintain Hermiticity in contrast to the Hamiltonian, i.e.,  $\mathcal{L}^\dagger \neq \mathcal{L}$ . The Hamiltonian contributions in Eq. (3) are still Hermitian, factoring out the imaginary unit  $i$ .  $L_\nu^\dagger L_\nu \otimes \mathbb{I}$  and  $\mathbb{I} \otimes (L_\nu^\dagger L_\nu)^T$  are Hermitian themselves, but not with the additional  $-i$  factored out from the Hamiltonian.  $L_\nu \otimes (L_\nu^\dagger)^T$  is not necessarily Hermitian in itself or with an additional  $-i$ . In the following, we briefly discuss the adaptations for each method with regards to the closed system MPS implementation.

#### 4. Krylov-Arnoldi subspace method

The Krylov approximation [54, 57–59] directly builds the new state after the time step  $dt$  evaluating the product  $\exp(\mathcal{L}dt) |\psi\rangle$ . The exponential taken within the Krylov subspace is much smaller than the dimension of the Hilbert space or Liouville space scaling with  $d^L$  and  $d^{2L}$ , respectively. The exponential in the Krylov subspace is used to approximate the new state after the time step; thus, the exponential does not represent a propagator. We recall that in case of a Hamiltonian, which is by definition Hermitian, the matrix to be exponentiated in Krylov subspace is tridiagonal. We label it Krylov-Lanczos in analogy to the Lanczos eigenvalue algorithm for Hermitian matrices. In contrast, the Liouville operator may violate Hermiticity, and we use the Krylov-Arnoldi algorithm. We use the name Krylov-Arnoldi due to the similarity with the Arnoldi algorithm solving for eigenvalues of a non-Hermitian matrix. Both variants of the algorithm construct a set of orthogonal Krylov vectors  $\{\mathbf{v}_\eta\}$ ,  $\eta = 0, \dots, M$  from the powers of the operator, i.e., Hamiltonian or Liouville operator. The number of Krylov vectors  $M$  is determined based on a tolerance and much smaller than the complete space, e.g.,  $d^{2L}$  for the Lindblad master equation. The initialization of the Krylov vectors and the iterative construction follows

$$\mathbf{v}_0 = |\psi\rangle, \quad \mathbf{v}_0 = \frac{|\rho\rangle\rangle}{\langle\langle\rho|\rho\rangle\rangle}, \quad (16)$$

$$\mathbf{v}'_{\eta+1} = H\mathbf{v}_\eta, \quad \mathbf{v}'_{\eta+1} = \mathcal{L}\mathbf{v}_\eta, \quad (17)$$

where  $\mathbf{v}'_\eta$  have to be orthogonalized against the previous Krylov vectors to obtain  $\mathbf{v}_\eta$ . Taking a step back from the details, one observes that this procedure is well-defined in terms of tensor networks. The application of the Hamiltonian or Liouville operator represented as an MPO to a quantum state can be either executed via a contraction followed by a compression or fitting a state while minimizing the distance. The orthogonalization depends of the overlap of two vectors represented as an MPS or MPDO, which is a standard implementation for measuring distances between pure states. In a second step, the vectors weighted with the overlap have to be subtracted from  $\mathbf{v}'_\eta$ . Sums of MPSs or MPDOs can be calculated variationally minimizing the distance again; an actual sum increases the bond dimension and requires compression becoming inconvenient beyond a few terms in a sum. The variational methods to achieve these steps are explained for example in [54].

So far, we have constructed the Krylov vectors but not propagated the quantum state, MPS or MPDO, for one time step  $dt$ . A detailed description of the construction of the Krylov matrix  $M_K$  and proof of validity is beyond the scope of this work, and we refer to the corresponding literature [57, 60, 61]. The Krylov matrix is constructed from the overlaps of  $\mathbf{v}_\eta$  and is sparse, i.e., tridiagonal (upper Hessenberg) for a Hermitian Hamiltonian (Liouville operator). We introduce the exponential

$$P_K = e^{-iM_K dt}, \quad P_K = e^{M_K dt}. \quad (18)$$

The  $i^{\text{th}}$  row and  $j^{\text{th}}$  column is specified with  $(P_K)_{i,j}$ . The new state propagated from  $t$  to  $t + dt$  is then defined as

$$|\psi\rangle = \sum_{i=0}^M (P_K)_{i,0} v_i, \quad |\rho\rangle\rangle = \sum_{i=0}^M (P_K)_{i,0} v_i. \quad (19)$$

The two final numerical steps include the implementation of the matrix exponential in Eq. (18) and the summation in Eq. (19) to build the new state. The first is solved for the Lindblad master equation with a general matrix exponential handling the upper Hessenberg matrix  $M_K$ ; the Hamiltonian version can profit from using the tridiagonal Hermitian structure in  $M_K$  and reflects the main difference between the implementation of the Lindblad master equation in contrast to the Schrödinger equation. In theory, one can use the Krylov-Lanczos algorithm as a fallback for Hamiltonian mixed state evolutions when handling the imaginary unit  $i$  accurately. The update of the state is a sum over MPS or MPDOs and can be solved as aforementioned in the orthogonalization. In summary, the MPDO representation is convenient in combination with representing the MPO in Liouville space; all methods except the exponential of the Krylov matrix can be reused without further modification, keeping an implementation cheap.

#### 5. Local Runge-Kutta

The local Runge-Kutta (LRK) method is another method allowing us to evolve Hamiltonians with long-range interactions [55]. The version for the Schrödinger equation takes the MPO of the Hamiltonian and calculates an MPO representation of the propagator for the corresponding time step. The propagator MPO has a smaller bond dimension, by one, and is an efficient representation. It can either be contracted to obtain the new state or fitted. The steps to obtain the MPO of the propagator involve an intermediate mapping to hard-core bosons. A generalization to the non-Hermitian Liouville operator including non-local Lindblad operators is beyond this work here. But we can use the specific structure of the MPO for the propagator to generalize it at least to local Lindblad operators and their representation in Liouville space.



Therefore, we look at the operator-valued MPO matrix of the propagator  $W^{II}$  consisting of operator-valued four sub-matrices with subscript  $A$ ,  $B$ ,  $C$ , and  $D$ :

$$W^{II} = \begin{pmatrix} W_D^{II} & W_C^{II} \\ W_B^{II} & W_A^{II} \end{pmatrix}, \quad (20)$$

Every term expect  $W_D^{II}$  involves the mapping to hard-core bosons; therefore, we do not describe  $W_A^{II}$ ,  $W_B^{II}$ , and  $W_C^{II}$  as their definition does not change for local Lindblads and details can be found in [55].  $W_D^{II}$  contains all local site terms and is simply the exponential of these local terms, i.e., the propagator of a system truncating all interactions. For example, this local site term is the coupling to the transverse field in the quantum Ising model with a Pauli matrix or the number operator  $n_k$  acting on site  $k$  and the on-site interaction  $n_k(n_k - 1)$  for the Bose-Hubbard model with appropriate weight for both cases. In the implementation of the Schrödinger equation,  $D$  is the sum over all site rules for site  $k$  and therefore Hermitian. The corresponding exponential uses this fact. If the Lindblad operators are local, the Lindblad operators can be included entirely in this term  $D$  in the MPDO approach. The exponential has then to be calculated for a general matrix because the Lindblad terms  $L_\nu \otimes L_\nu^*$  do not necessarily enforce Hermiticity. Since the other terms are not affected by the local terms, they can stay in place as they are.

Evidently, this approach only works for local Lindblad operators. To what extent non-local Lindblad operators are covered by the method remains a subject of future research. Moreover, the current implementation makes the symmetric tensor to the full space and back to calculate the representation for the LRK-propagators. For that reason, the symmetry implementation only needs to consider a correct mapping.

## 6. Time-Dependent Variational Principle

The TDVP [56, 62] is the third evolution method based on the MPO. Its elegance is the elimination of errors depending on the time step  $dt$  for time-independent Hamiltonians; remaining errors are an insufficient bond dimension or discretizing a time-dependent Hamiltonian in time. The algorithm itself benefits from approaches used widely in other tensor network algorithms, namely effective Hamiltonians from a variational ground state search and similarities to the KTEBD algorithm. The differences from a Hamiltonian evolution and the Liouville operator have to be considered for its adaption. We point out that there is another time evolution using directly a variational approach which minimizes the distance between a guess for the new density matrix and the time-evolved density matrix [63].

Based on the suggested TDVP algorithms with a single-site update or a two-site update, we use for our analysis the two-site version. The advantages are the possibility for a growing bond dimension and the automatic introduction of new symmetry sectors, which may not be present in the initial state. The latter is, for example, important if the initial state is defined as a product state, e.g., Fock state in the Bose-Hubbard model. Reference [56] derives in detail that the time evolution is then defined in terms of the time evolution under effective two-site operators and a backward time evolution of the single-site operators. For the Hamiltonian version, one has to be able to calculate

$$|\psi'\rangle = e^{-iH_{\text{eff}}^{[k,k+1]}dt} |\psi\rangle, \quad |\psi''\rangle = e^{+iH_{\text{eff}}^{[k+1]}dt} |\psi'\rangle. \quad (21)$$

Both can be efficiently computed, i.e., even without involving the variational methods used in Sec. III A 4, if the orthogonality center is contained in the sites  $(k, k + 1)$  for the two-site version and in  $k + 1$  for the single-site update; the corresponding tensors form a vector space. The corresponding term  $H_{\text{eff}} |\psi\rangle$  can be calculated; thus, we can use the Krylov subspace method relying on powers  $H_{\text{eff}}^n |\psi\rangle$  and update the corresponding two-site tensor for  $(k, k + 1)$  (one-site tensor for  $k + 1$ ) in the time evolution step (backward evolution). The TDVP method does not make use of the Hermitian property of the Hamiltonian, but requires the matrix exponential. The Krylov-Lanczos method with the tridiagonal matrix is used to calculate the propagator in the closed system case. The MPDO profits from its close similarity to the MPS. The Liouville operator is already represented as an MPO and  $\mathcal{L}_{\text{eff}}^{[k,k+1]}$  and  $\mathcal{L}_{\text{eff}}^{[k]}$  are constructed without any adaption. In contrast to the Hamiltonian in the Schrödinger equation, we have to take into account that  $\mathcal{L}$  is not hermitian; thus, the algorithm is again adapted for the Hessenberg matrix yielded by the Krylov-Arnoldi algorithm, and it is implemented in OSMPS. Section III A 4 explains the differences between the evolution under a Hermitian operator and a non-Hermitian operator with the Krylov method, which are independent of using the method with a global operator as in Sec. III A 4 or with an effective, local version as in the TDVP adaption. As an outlook, this upper Hessenberg matrix reappears when using the TDVP with the non-hermitian “effective” Hamiltonian of the quantum trajectories, where “effective” corresponds to the inclusion of dissipate terms and is further broken down into the “effective” Hamiltonian acting on two sites.

## 7. Time-Evolving Block Decimation

The TEBD [14] approach approximates the global propagator with local propagators; most implementation target nearest-neighbor Hamiltonians and the local propagators act on two sites. The global propagator  $\exp(\mathcal{L}dt)$  can use this technique. The

Suzuki-Trotter decomposition [64] then approximates the exponential of the Liouville operator as

$$e^{\mathcal{L}dt} = e^{\sum_{k=1}^{L/2} \mathcal{L}_{2k-1,2k} \frac{dt}{2}} e^{\sum_{k=1}^{L/2-1} \mathcal{L}_{2k,2k+1} dt} e^{\sum_{k=1}^{L/2} \mathcal{L}_{2k-1,2k} \frac{dt}{2}} + \mathcal{O}(dt^3) \quad (22)$$

where the formula in Eq. (22) represents the second order decomposition for an even system size; upper bounds of the sum over the site index  $k$  have to be adapted for odd system sizes. The scaling of the second order decomposition for a complete time evolution of  $n$  time steps and a total time  $T$  with  $T = n \cdot dt$  scales as  $\mathcal{O}(dt^2)$ . Higher orders of the decomposition can improve the scaling of the error which originates in the non-zero commutator of the terms in the set  $(2k-1, 2k)$  and the set  $(2k, 2k+1)$  at the cost of more terms. Notice that the commutators  $[\mathcal{L}_{2k-1,2k}, \mathcal{L}_{2k'-1,2k'}] = 0$  and  $[\mathcal{L}_{2k,2k+1}, \mathcal{L}_{2k',2k'+1}] = 0$  hold; thus, the sum of exponentials can be written as a product of exponentials of two-site terms representing the form used for the efficient numerical implementation. An alternative to the Trotter decomposition is the Sornborger decomposition [65], which has the same source of error, i.e., splitting a single exponential of non-commuting terms into multiple exponentials. This decomposition is the one used in the implementation in OSMPS.

The first and second release of OSMPS use a Krylov subspace method [57] for TEBD, which was argued to be slow [49] in comparison to the direct matrix exponential of the Hamiltonian in closed systems. We now have both methods implemented, with KTEBD and TEBD taking the matrix exponential of the Hamiltonian or Liouville operator, respectively. KTEBD follows closely the restriction of the Krylov method. Moving from Hermitian operators to non-Hermitian operators, the matrix in the Krylov subspace turns from symmetric tridiagonal to an upper Hessenberg form. We have to adapt the matrix exponential. Evidently, for taking the exponential of the Liouville operator, we also have to choose a matrix exponential for non-Hermitian matrices; we rely on LAPACK's ZGEEV. The symmetric MPDO profits from taking the exponentials of the block-diagonal structure. When building the block-diagonal structure, we ensure that every possible block is present by adding a  $0 \cdot \mathbb{I}$ , where  $\mathbb{I}$  is the identity operator of the corresponding subspace. An identity scaled with zeros adds the information about all present diagonal blocks without altering the matrix itself.

## 8. Measurements with overlaps

Measurements of the MPS representation profit immensely from the gauge installed, which reduces local measurements to operations on a single tensor. Similarly, correlations are only affected by the sites measured and all sites in between [15]. Unfortunately, MPDOs do not have such a benefit, and the complete tensor network has to be contracted to find the measurement outcome. Therefore, we define a few operations to allow us to obtain those measures. These operations are similar to the left-right overlaps and transfer matrices between two states in our MPS algorithms. In detail, we build the tensors  $L_{\alpha}^{[k-1]}$  and  $R_{\beta}^{[k+1]}$  such that the local measurements on site  $k$  of the operator  $O^{[k]}$  reduce to the contraction

$$\text{Tr}(\rho O^{[k]}) = \sum_{\alpha, i, i', \beta} L_{\alpha}^{[k-1]} B_{\alpha, (i, i'), \beta}^{[k]} O_{(i, i')}^{[k]} R_{\beta}^{[k+1]}. \quad (23)$$

The critical step is the initialization on the left and right end, respectively. We implement the concept which allows us to use general states, e.g., partially traced out MPS.<sup>1</sup> The three major steps are sketched in Fig. 2 for the left side of the tensor network. Figure 2 is an overview of the objective tracing out over site one and two and obtain a rank 1 tensor to be contracted with the rest of the system. First, we split the link to the left of the MPDO. This step is defined under the assumption that the link was created as a combined link. The correct decomposition can be stored; this link cannot change during any MPDO algorithm. If quantum numbers are present as in Fig. 2(b), we store the conserved quantities in the first half and fill the second half with zeros. This trick is necessary since the number of conserved quantities is an attribute of the tensor, not to a specific link. We contract over the local Hilbert space of the site in the next step, i.e., Fig. 2(c). The dimensions and quantum numbers of the original Hilbert space can be obtained from the identity operator. Transfer tensors for matrices in the bulk of the system are obtained via a contraction of the transfer tensor on the left, see Fig. 2(d), followed by the contraction of the local Hilbert space. We build the right overlap in an analog approach from the other side. This scheme corresponds in other words to the partial trace of selected sites in the density matrix.

## B. Quantum Trajectories

Quantum trajectories follow the idea that any mixed quantum state can be sampled and written via an ensemble of pure states

$$\rho = \sum_i |\phi_i\rangle \langle \phi_i|. \quad (24)$$

<sup>1</sup> Such an approach is beneficial for the following example: (i) Obtain MPS via ground state or time evolution. (ii) Trace out over a subsystem followed by (iii) a conversion to an MPDO.

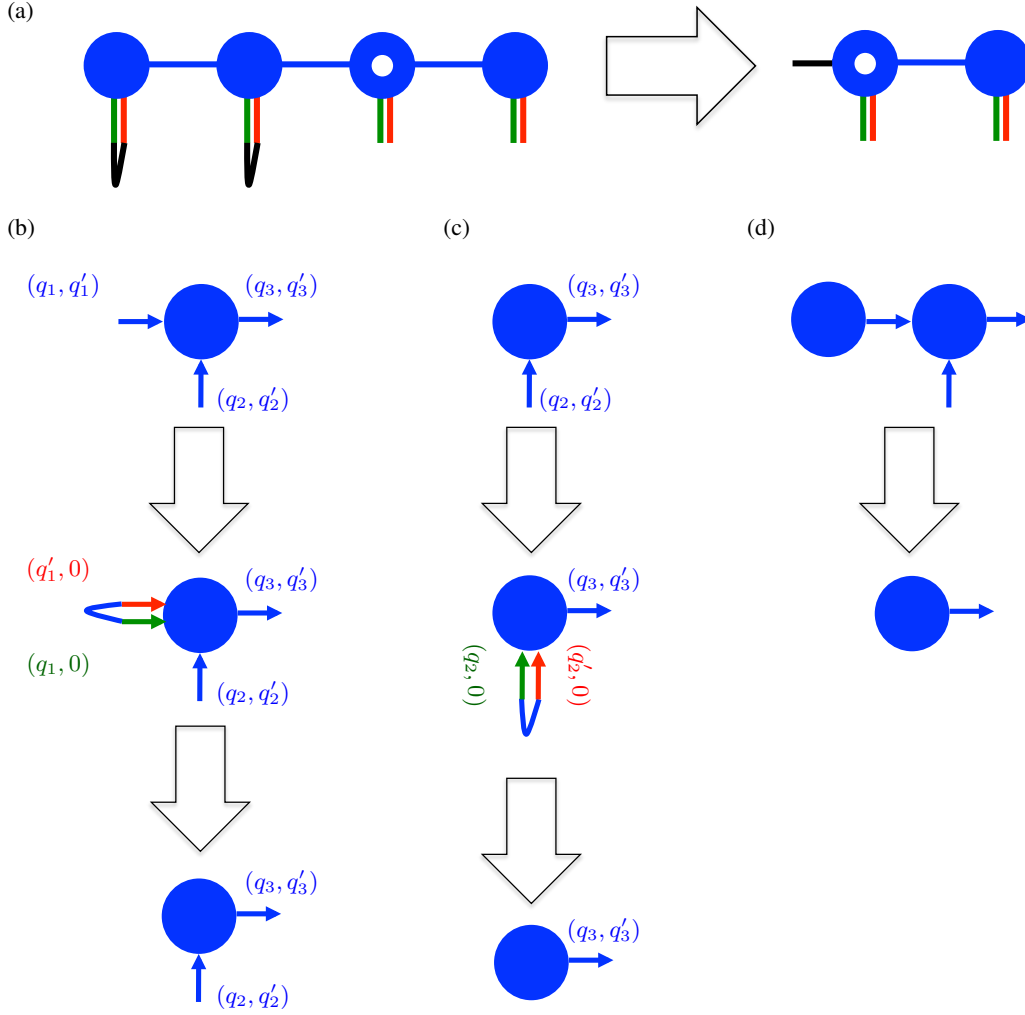


Figure 2. *Left transfer tensor for an MPDO.* The left transfer tensor for the  $k^{\text{th}}$  site is built by taking a partial trace of the sites  $1, \dots, k-1$ . (a) We first split and then contract the local Hilbert spaces on the sites 1 and 2 corresponding to a partial trace, see black curves. The results left transfer tensor of rank 1 is also shown in black on the right. the first site is built with the following steps. (b) Contract incoming link to the left by splitting the link into its original underlying links. Then, (c) Contract the local Hilbert space after splitting it. The transfer tensors for sites  $k \geq 2$  can be built with subsequent steps (c) Contract the transfer tensor from the site  $k-1$  and (d) again.

The essential points of the implementation are the effective, non-Hermitian Hamiltonian and the sampling over the different trajectories. The latter are well covered with the data parallelism via MPI present in the package; from the point where the number of trajectories is specified, they are spread across all possible cores as any other set of simulations in OSMPS, e.g., ground state searches for different system sizes. The non-Hermiticity of the effective Hamiltonian can be addressed analogously to the MPDO cases but on the level of the Hilbert space and pure quantum states. The effective Hamiltonian  $H_{\text{eff}}$  derived from Eq. (1) is

$$H_{\text{eff}} = H - \frac{i\hbar}{2} \sum_{\nu} L_{\nu}^{\dagger} L_{\nu}. \quad (25)$$

This effective Hamiltonian  $H_{\text{eff}}$  violates Hermiticity and conservation of norm when used in the Schrödinger equation. The latter has its use on the decision on when to apply the Lindblad operators to the system. The non-Hermiticity leads to changes in the time evolution methods as discussed in the previous section for the MPDO. The Krylov method, TDVP, and KTEBD switch from Krylov-Lanczos to Krylov-Arnoldi approximation of the new state. TEBD uses a function for non-Hermitian matrices to exponentiate  $H_{\text{eff}}$ . The LRK method has to use a non-Hermitian matrix exponential for the local terms but has one additional problem. LRK itself does not conserve norm which enhances or prevents the loss of norm due to  $H_{\text{eff}}$ .

It remains to present the actual algorithm for the trajectories, which is described in many places [38], but reviewed here briefly for completeness. While looping over the time steps of the evolution, we execute the following steps: (i) Draw a random number

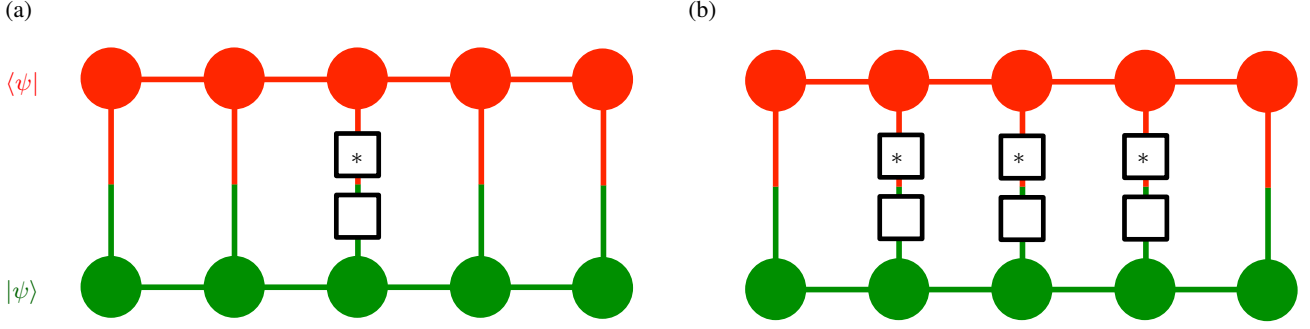


Figure 3. *Contraction for unweighted probabilities in quantum trajectories.* (a) Local Lindblad operators obtain their weight by a measurement of norm after contracting it to the current quantum state. This step can be reduced to a single site operation. (b) The many-body string Lindblad terms, here shown for three sites, need to contract the local operators with the state for each site before measuring the norm, i.e., the unweighted probability.

$r_{\mathcal{N}} \in \mathcal{U}(0, 1)$  and ensure the state  $|\psi(t=0)\rangle$  is normalized at the beginning. The uniform distribution between 0 and 1 is written as  $\mathcal{U}(0, 1)$ . This normalization is necessary as the decreasing norm of  $|\psi(t)\rangle$  is used in the following steps. (ii) Calculate time steps under  $H_{\text{eff}}$  without renormalizing the state. (iii) Measure the norm  $\mathcal{N}$  of the state. If  $\mathcal{N} < r_{\mathcal{N}}$ , then we apply a quantum jump according to the steps (a) through (c) described below. Otherwise, we continue to the next step in the time evolution, i.e. (i). The steps to select a random quantum jump are the following. (a) Calculate unweighted probabilities for each Lindblad operator  $L_{\nu}$  as  $p_{\nu} = \langle \psi | L_{\nu}^{\dagger} L_{\nu} | \psi \rangle$ . Figure 3 shows the contractions to obtain the  $p_{\nu}$ 's for the two types of Lindblad operators implemented in the package. (b) We normalize  $p_{\nu}$  to  $P_{\nu} = p_{\nu} / \sum_{\nu} p_{\nu}$ . (c) We draw a random number  $r_{\kappa} \in \mathcal{U}(0, 1)$ . We apply to the state the Lindblad operator  $L_{\kappa}$  such that  $P_{\kappa-1} < r_{\kappa} \leq P_{\kappa}$  holds. The state is renormalized after application of the Lindblad operator  $L_{\kappa}$  and we continue the time evolution with step (i).

It is worthwhile to take a look at the measurement procedure for QTs. Local measurements or correlations can be averaged over all trajectories with equal weight. For example, a local observable  $\langle O_k \rangle$  is calculated for QTs as

$$\langle O_k \rangle = \frac{1}{N_{\text{QT}}} \sum_{j=1}^{N_{\text{QT}}} \langle O_k \rangle_j, \quad (26)$$

where  $N_{\text{QT}}$  is the number of trajectories and  $\langle O_k \rangle_j$  is the observable of the  $j^{\text{th}}$  trajectory. Here, we use the concept that the density matrix is a statistic ensemble of pure states  $\rho = \sum_j p_j |\psi_j\rangle \langle \psi_j|$  with equal probabilities  $p_j = 1/N_{\text{QT}}$ . Obviously, this approach does not work for all observables; the purity  $\mathcal{P}$  of each  $|\psi_j\rangle$  is equal to one, but the purity of the density matrix is not necessary the average, i.e., one. We can calculate the purity as

$$\mathcal{P} = \text{Tr} [\rho^2] = \sum_{j,j'=1}^{N_{\text{QT}}} \frac{1}{N_{\text{QT}}^2} \text{Tr} [|\psi_j\rangle \langle \psi_j| |\psi_{j'}\rangle \langle \psi_{j'}|], \quad (27)$$

where each of the  $N_{\text{QT}}^2$  traces can be represented as contraction across a tensor network. But this measurement goes beyond simple MPI parallelization as the measurement needs all states at the time of the measurement and a posteriori averaging is not possible. We can extend this argument to any term with power differing from first order in  $\rho$ . Therefore, non-linear measures need all trajectories for measuring, which can either be achieved with saving each state or while waiting until all trajectories have reached the measurement.

### C. Locally Purified Tensor Networks

LPTN time evolution relies on the Trotter decomposition and Kraus operators applied to the purification of the density, as previously outlined in Reference [33]. Therefore, we restrict the description to the technical implementations used within OSMPS. We start with a brief description of the construction and continue with open system decomposition. We conclude with the setup for finite temperature. The current implementation is restricted to nearest-neighbor interaction in the Hamiltonian and local Lindblad operators. Furthermore, no symmetries are present.

### 1. Construction of Locally Purified Tensor Networks

We focus on the conversion of MPS to LPTN and the definition of the infinite temperature density matrix  $\rho_\infty$ . The conversion from an MPS tensor  $A_{\alpha,i,\beta}^{[k]}$  representing site  $k$  to an LPTN tensor is as simple as inserting an additional link of dimension 1, i.e.,  $B_{\alpha,i,\kappa,\beta}^{[k]}$ . The local tensors for the definition of  $\rho_\infty$  have the link dimension  $(1, d, d, 1)$  and are diagonal in the entries

$$B_{\alpha,i,\kappa,\beta}^{[k]} = \delta_{i,\kappa}. \quad (28)$$

### 2. Trotter decomposition for open systems

The evolution of an LPTN separates the Hamiltonian part of the Liouville operator  $\mathcal{L}$  from the dissipative part  $\mathcal{D} = \sum_\nu L_\nu \rho L_\nu^\dagger - \frac{1}{2} \{L_\nu^\dagger L_\nu, \rho\}$  in a second order Trotter decomposition. The exponential of the time evolution is approximated with

$$e^{\mathcal{L}dt} \approx e^{-\frac{i}{\hbar}[H,\rho]\frac{dt}{2}} e^{\mathcal{D}dt} e^{-\frac{i}{\hbar}[H,\rho]\frac{dt}{2}}. \quad (29)$$

The Hamiltonian contribution evolves each part of the purification  $\rho = XX^\dagger$ , where it is sufficient to propagate  $X$ . The Hamiltonian itself is approximated with two-site propagators in a Sornborger decomposition [65]. We remain with the dissipative part, which we express as Kraus operators:

$$e^{\mathcal{D}dt} |\rho\rangle\rangle = \sum_{\nu'} K_{\nu'} X X^\dagger K_{\nu'}^\dagger = \sum_{\nu'} (K_{\nu'} X)(K_{\nu'} X)^\dagger. \quad (30)$$

We recall that the local Kraus operators keep the locally purified tensor network in its form. We generate the Kraus operators from the first order approximation [44]

$$e^{\mathcal{D}dt} |\rho\rangle\rangle = \sum_{\nu'=0}^N K_{\nu'} \rho K_{\nu'}^\dagger + \mathcal{O}(dt), \quad (31)$$

$$K_{\nu'=0} = \mathbb{I} - \frac{dt}{2} \sum_{\nu=1}^N L_\nu^\dagger L_\nu, \quad (32)$$

$$K_\nu = \sqrt{dt} L_\nu, \nu = 1, \dots, N. \quad (33)$$

Alternatively, we can decompose the exponential of the Liouville operator into Kraus operators. The contraction of the Kraus operators increases the auxiliary dimension  $\kappa$  to a larger  $\kappa' = \kappa(N+1)$ . The dimension is reduced in a truncation similar to the truncation when splitting nearest neighbor sites.

### 3. Imaginary time evolution for finite- $T$ states

The finite temperature states according to the Gibbs distribution are generated in an imaginary time evolution starting from the infinite temperature state  $\rho_\infty$  as explained in Sec. III A 2. As evolution is purely Hamiltonian and does not contain any dissipative part  $\mathcal{D}$ , we can reuse the decompositions for MPS/MPDO methods. Both second and fourth order Sornborger approximations are available.

## IV. SIMULATION SETUP AND CONVERGENCE

We describe the convergence of the different scenarios in the next three subsections. We start with the analysis of the finite- $T$  states in Sec. IV A; we use the quantum Ising model as example. Then, we move to the Lindblad master equation and consider simulations without and with symmetry. Section IV B considers the dissipative dynamics of an exciton for the convergence study of a system without conserved symmetry. The transient dynamics of the Bose-Hubbard model with number conservation are described in Sec. IV C.

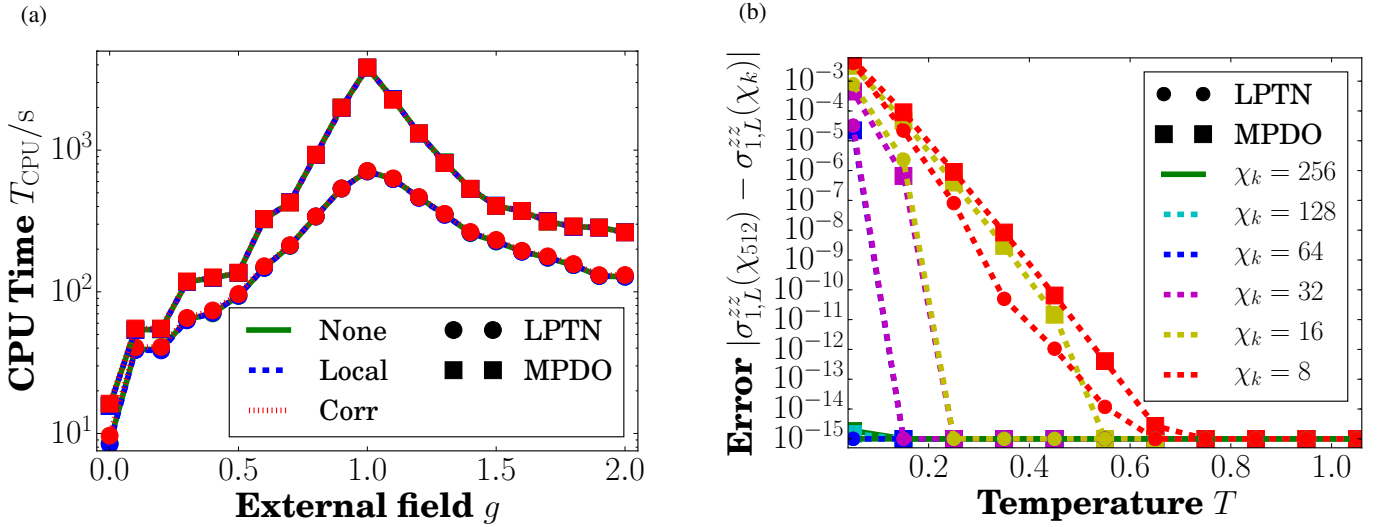


Figure 4. *Performance of finite-T simulations.* We consider the quantum Ising model without  $\mathbb{Z}_2$  symmetry to study basic convergence of the finite-T states represented by LPTNs and MPDOs. The system size for the simulations is  $L = 100$ . (a) The CPU times  $T_{\text{CPU}}$  for different measurements indicate that LPTNs are favorable for this model. The bond dimension is  $\chi = 512$ . The measurements are not the major cost and all three curves for “None”, “Local”, and “Corr” overlap. (b) We compare the error of the  $zz$ -correlation measurement between the first and last site to the most accurate result with  $\chi = 512$ . Data points, especially circles for MPDOs, may hide behind other data points of lower bond dimension for the error level  $10^{-15}$ . We conclude from the lower errors for the same bond dimension that LPTNs use their bond dimension more efficiently in this example.

#### A. Finite-T states in the Ising model (MPDO and LPTN)

We now turn to finite temperature states according to the Gibbs distribution and their convergence. We compare LPTNs and MPDOs; quantum trajectories cannot simulate finite temperature states. We take the quantum Ising model defined in Eq. (10) as an example. The comparison is restricted to the TEBD2 time evolution methods and the overall Hilbert space without addressing a specific sector in the  $\mathbb{Z}_2$  symmetry.

Figure 4 answers two important questions: which method needs less CPU time to run the simulations and which network type uses its bond dimension more efficiently? The first answer is important to use computational resources in the best possible way whenever both tensor networks can be applied to the problem. The second question can deliver a partial answer as to which is the most favorable network to store entanglement for any state similar to those finite-T states. We consider the finite-T evolution with the first measurements at  $T = 1.05$  and the last measurement at  $T = 0.05$  in steps of  $\Delta T = 0.1$ . We use a time step  $dt = 0.01$ , and additional steps  $dt' < dt$  to reach the measurements at the corresponding temperatures. The temperatures are in units of the interaction  $J$ , and we have a unitless  $k_B = 1$ .

We first discuss Fig. 4(a) and the computational effort for the imaginary evolution and the measurements. We choose a system size of  $L = 100$ , a maximal bond dimension  $\chi = 512$ , and three type of measurements: (i) only default measurements as the energy; and (ii) default measurements and two local observables, i.e.,  $\sigma_j^x$  and  $\sigma_j^z$ . (iii) The last type of simulations computes the default measurements, the local measurements presented previously, and the correlations of the Pauli matrices in the  $x$ - and  $z$ -direction. All simulations are carried out on a *Penguin Relion 1752DDR/QSFP 2x(Intel X5675) 12 cores 3.06 GHz*. The peak of the CPU time  $T_{\text{CPU}}$  is located around the critical point; the entanglement is maximal at the critical point of the Ising model, i.e.,  $g = 1.0$ . We see a clear difference between the LPTN and MPDO times for no measurements, which is related in aspects to the computational scaling of the underlying operations. LPTNs build the two-site Hamiltonian on a  $d^2 \times d^2$  matrix, where the local dimension  $d$  is equal to two in the qubit example. In contrast, the Hamiltonian represented in Liouville space is of dimension  $d^4 \times d^4$ . The contraction of a single two-site propagator with a two-site tensor then scales as  $\chi^2 d^6$  for the LPTN and  $\chi^2 d^8$  for the MPDO. We remark that our MPDO implementation could be further optimized using the fact that the commutator  $[H \otimes \mathbb{I}, \mathbb{I} \otimes H^T] = 0$ . Thus, we can simplify the action of the two site propagator in Liouville space to  $\exp(H \otimes \mathbb{I} + \mathbb{I} \otimes H^T) = (\exp(H) \otimes \mathbb{I})(\mathbb{I} \otimes \exp(H^T))$ . Each exponential can be applied separately in two steps with a scaling of  $\chi^2 d^6$  for each contraction. However, this approach would in our eyes defeat the purpose of an MPDO, which is representing the density matrix as an MPS; but here, the link of the local dimension has to remain split throughout the complete evolution. Synergy effects between the MPDO and MPS implementation would be decreasing. The measurements, executed in addition to the imaginary time evolution, increase computation time where they are beyond fluctuations. LPTNs tend to have less cost for measurements as local and quasi-local measurements do not have to contract the complete tensor network. But

overall, the selected measurements are not the significant costs in these simulations.

Figure 4(b) describes the error for different bond dimensions in comparison to the most accurate bond dimension. We choose this most accurate bond dimension as  $\chi_{\max} = 512$ . The system size is  $L = 100$ , and we set the transverse field to  $g = 1.0$  maximizing the possible entanglement in the quantum Ising model. The correlation is among the observables most affected by a limited bond dimension; therefore we consider

$$\epsilon_{zz} = |\langle \sigma_1^z \sigma_L^z \rangle_{\chi_{\max}} - \langle \sigma_1^z \sigma_L^z \rangle_{\chi}|, \quad (34)$$

where  $\chi < \chi_{\max}$ . We see a decreasing error  $\epsilon_{zz}$  as the bond dimension  $\chi$  approaches  $\chi_{\max}$  for both LPTN and MPDO. This behavior is expected. But we also observe that each curve representing the LPTN has a smaller error than the corresponding MPDO curve. Assuming that the simulations with the highest bond dimension are both converged and yield the correct results, LPTNs use the bond dimension more efficiently than MPDOs. This statement is supported by the error in the energies for the final temperature. The LPTN has a maximal absolute error of  $2.09 \cdot 10^{-5}$  for  $L = 100$ ,  $\chi = 512$ ,  $g = 1.0$ , while the error for the MPDO yields  $6.21 \cdot 10^{-4}$ . Thermal energies for low enough temperatures can be calculated via the eigenvalues of Majorana Hamiltonian after the Jordan-Wigner transformation; energies of excited states  $E'$  are truncated if  $\exp(-(E' - E_0)/T) < 10^{-16}$  and avoids iterating over all  $2^L$  eigenenergies. This effect might also contribute to the CPU times observed. Lower bond dimension leads to the use of less computational resources. Unlike a variational or imaginary time ground state search, we cannot stop the algorithm at a defined precision and compare the CPU times.

One may ask where the speed-up of the LPTN in comparison to the MPDO occurs and how it scales with system size. This question is in relation with the known growth of entanglement associated with quantum critical phenomena [66, 67]. We consider the system sizes  $L \in \{100, 150, 200\}$  at the critical point  $g = 1.0$  for the scenario with local measurements at bond dimension  $\chi = 512$ . We compare the ratio  $r$  of MPDO over LPTN from measurement 1 to 10 and 10 to 11 according to the time stamp of the results files. We obtain the ratios  $r(L) = \{4.17, 4.38, 4.36\}$  for ascending system sizes, and  $r(L) = \{5.52, 6.00, 6.13\}$  are the ratios between the measurements 10 and 11. We observe the trend that the speed-up has a larger contribution at the end of the time-evolution and increases with system size. We point out that the major part of the time evolution takes place for the last data points due to the inverse relation of temperature to evolution time. In conclusion for the finite-T simulations, LPTNs scale better in the scenario of the quantum Ising model. The maximal difference in CPU time is around the critical point and suggests that LPTNs support entanglement better for imaginary time evolutions.

## B. Local Lindblad operators without symmetry (QT, MPDO, and LPTN)

Lindblad equations without conserved quantities and local channels have a variety of applications reaching from the quantum Ising model with local spin flips over XXZ model transport problems using local channels at both end of the chains [68] to lossy photon cavities. We choose to simulate the transport of an exciton with the initial condition and Hamiltonian based on reference [69, 70]. Examples of the Lindblad operators for transport problems can be motivated from [71], which describes energy loss and dephasing noise in molecular structures. We consider the Hamiltonian

$$H = J \sum_{k=1}^{L-1} b_k b_{k+1}^\dagger + h.c. + \Delta \sum_{k=1}^L n_k - \mu \left( b_k^\dagger + b_k \right), \quad (35)$$

and  $J$  is the tunneling strength,  $\Delta$  an on-site potential, and  $\mu$  the driving due to the electromagnetic field. The latter is turned off on all sites for all simulations, i.e.,  $\mu = 0$ . The corresponding Lindblad master equation with loss of a strength  $\gamma$  and dephasing, coupled with  $\gamma_d$ , is defined as

$$\frac{\partial}{\partial t} \rho = -\frac{i}{\hbar} [H, \rho] + \sum_{k=1} \gamma \left( b_k \rho b_k^\dagger - \frac{1}{2} \{ b_k^\dagger b_k, \rho \} \right) + \sum_{k=1} \gamma_d \left( n_k \rho n_k - \frac{1}{2} \{ n_k n_k, \rho \} \right). \quad (36)$$

We define the initial state  $|\psi(t=0)\rangle$  as a product state on three subsystems  $A$ ,  $B$ , and  $C$ , i.e.,  $|\psi(t=0)\rangle = |\psi(t=0)\rangle_A \otimes |\psi(t=0)\rangle_B \otimes |\psi(t=0)\rangle_C$ . The subsystems  $A$  and  $C$  are in the vacuum state  $|\psi(t=0)\rangle_A = |0 \dots 0\rangle$  and  $|\psi(t=0)\rangle_C = |0 \dots 0\rangle$ , respectively. Subsystem  $A$  contains  $L_A$  sites; subsystem  $C$  spans  $L_C$  sites. The initial exciton is defined via the relation from [70] on the subsystem  $B$  with a size of  $L_B$  sites:

$$|\psi(t=0)\rangle_B \propto \sum_{k=L_A+1}^{L_A+L_B} e^{ik_0 k a} e^{-a^2(k-k_0)^2/(2\sigma^2)} b_k^\dagger |0 \dots 0\rangle. \quad (37)$$

Thus, the total system has a system size of  $L = L_A + L_B + L_C$  sites. The exciton on subsystem  $B$  is not a product state and has entanglement. It can be constructed on the completed Hilbert space and decomposed via SVDs to an MPS. This approach

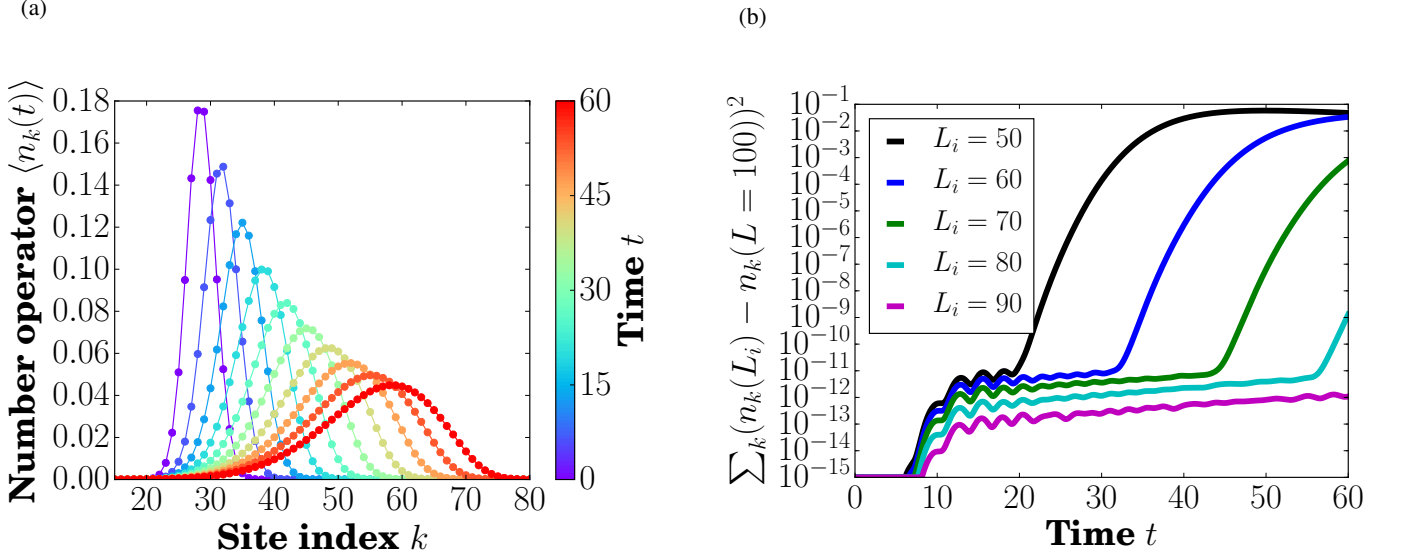


Figure 5. *Exciton dynamics with open boundary conditions.* (a) The dynamics of the largest system with  $L = 100$ . The initial wave package loses height while spreading out. (b) We consider different system sizes  $L$  to estimate when the reflection of the exciton returns from the boundary at site  $k = L$ . The exciton is initially in the sites  $k = 11, \dots, 40$  and moving right. System sizes of  $L = 60$  ( $L = 90$ ) are sufficient to simulate the closed system for a time of  $t = 30$  ( $t = 60$ ). Times are in the unit of the local term  $\Delta$ .

is limited to about 24 sites and supported by the OSMPS Python interface. On the other hand, we can write the state as a sum of MPSs, where each state in the sum of Eq. (37) has a bond dimension of 1. We compress this MPS yielded by the summation, which scales better with larger  $L_B$ . Figure 5(a) pictures the exciton at different points in time and we observe a loss of height while spreading out in the closed system. We are well aware that this setup of the problem has problems from the back reflection of the exciton at the boundary  $k = L$ . Therefore, Fig. 5(b) shows the deviation of the exciton's mean position for different system sizes for the closed system over time in comparison to  $L = 100$ . We see small errors at the order of  $10^{-12}$  and do not concentrate on these errors as  $10^{-12}$  is at the order of truncated singular values. We conclude that a system size of  $L = 90$  is sufficient for an evolution time  $\tau = 60$  without considering reflections from the boundary. To estimate the error, we look at the number operator  $N(t) = \sum_{k=1}^L n_k(t)$  as

$$\epsilon_{N(t)} = |N(t) - N(0) \exp(-\gamma t)|, \quad (38)$$

where the relation  $dN(t)/dt = -\gamma N(t)$  can be easily derived when considering the commutation relation between  $b_k, b_{k'}^\dagger$  and  $n_{k''}$  as well as  $d/dt N(t) = d/dt \text{Tr}[N\rho(t)] = d/dt \text{Tr}[Nd/dt\rho(t)]$ . This property is one result which can be checked besides convergence regarding the bond dimension or other convergence parameters. We start with an analysis of the momentum of the exciton; the position of the maximum of the exciton, the mean, the standard deviation, and the skewness give a good impression of the dynamics, see Fig. 6(a). We observe that for a coupling  $\lambda = \lambda_d = 0.05$  the position of the maximum remains almost equal to the closed system case. The mean, i.e., "center of mass", propagates at a slower speed in the open system in comparison to the closed system. This trend is reflected in the increased standard deviation and skewness of the exciton. These measures can be used for a more detailed analysis of the open system dynamics of the exciton, but we turn to the evaluation of the different tensor networks and algorithms.

Figure 6(b) shows the error in the number of excitations, which decays exponentially according to Eq. (38). TDVP has the lowest error; TEBD has a local minimum of the error around  $t \approx 10$  switching between under- and overestimating the number of excitations in the system and recovers the envelope otherwise in our understanding. The LRK has an error similar to TEBD. In the long time limit, all of these three algorithms using MPDOs have a similar error. The Krylov method has an error about an order of magnitude bigger at the beginning and recovers the error of the other algorithms in the long-time limit; it is not considered an option in our opinion. If we consider the second tensor network, LTPN, the error is the largest in the long-time limit. If we consider in addition the CPU times in Fig. 6(d) for each simulation as a function of the maximal bond dimension, we can get a much better picture as to what method is best suited to the problem. Two things become evident. (i) The Krylov method for MPDOs is two orders of magnitude slower than the next slowest algorithm for MPDOs. The other algorithms reach a saturation of the CPU time, and we conclude that they do not exceed the maximal bond dimension. Otherwise, TEBD is preferable when applicable. For long-range interactions in the Hamiltonian, LRK is preferable over TDVP from a resource viewpoint. (ii) The LTPN algorithm requires much higher resources in comparison to MPDO methods. We remind the reader that a maximal bond dimension  $\chi_{\max} = \kappa = 32$  leads to a bond dimension of  $32^2$  in many tensor operations due to the auxiliary link in the local tensors of the same dimension. This approach is fair when comparing the splitting of a two-site tensor when



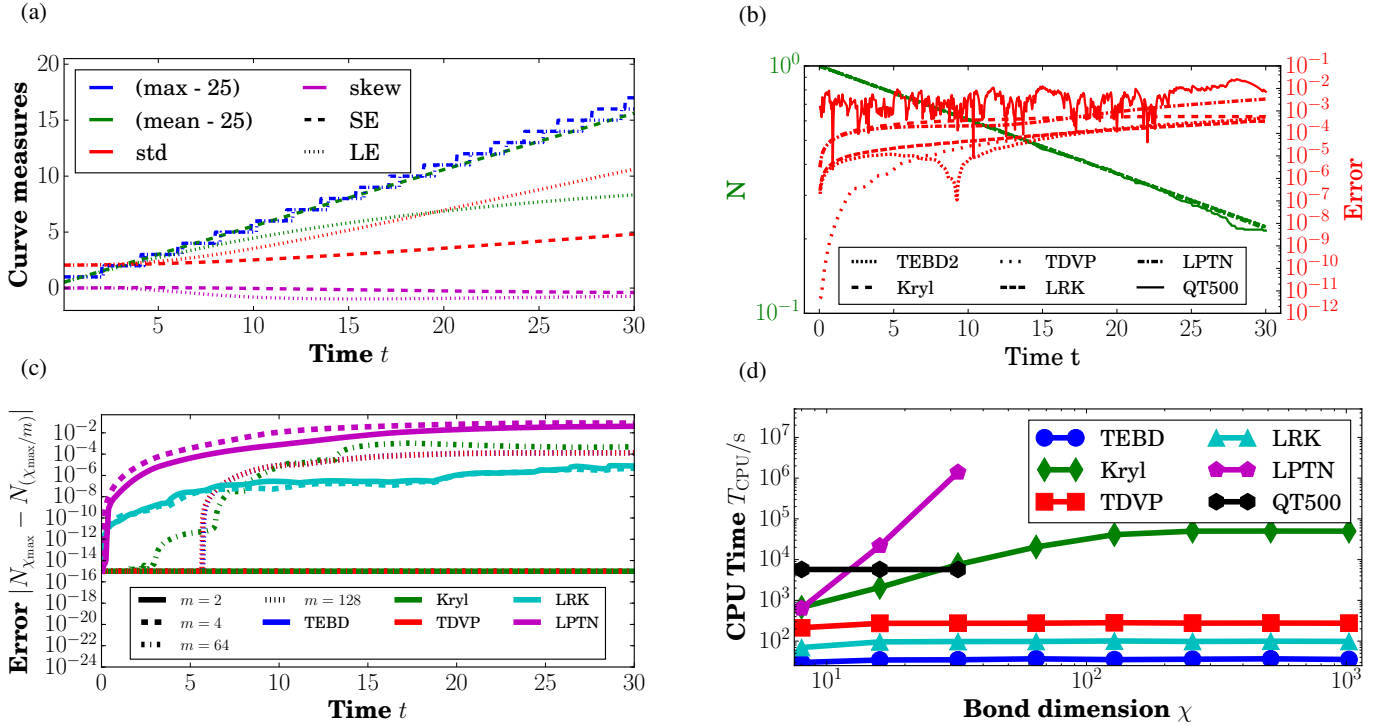


Figure 6. *Convergence of open quantum system exciton dynamics.* (a) The different momenta of the exciton capture best the effects of the dephasing. Although the maximum (max) of the exciton almost stays constant, the mean (mean), standard deviation (std), and skewness (skew) capture the dynamics of the Lindblad equation (LE) with coupling  $\lambda = \lambda_d = 0.05$  very well, shown side-by-side with the Schrödinger equation (SE). (b) The coupling to the decay Lindblad operator induces an exponential decay of the total number of particles in the excited state. All time evolution methods reproduce this exponential decay (green); thus, we show the corresponding error (red). The TDVP for MPDO works best. (Linestyles in the legend are used for green and red curves.) (c) We show how efficiently the bond dimension is used by comparing the convergence of  $N(t)$  for the different bond dimension to the maximal bond dimension, i.e.,  $\chi_{\max}^{\text{MPDO}} = 1024$  and  $\chi_{\max}^{\text{LPTN}} = \kappa_{\max} = 32$ . MPDO simulations with TEBD and TDVP use the bond dimension very efficiently for this problem and already show no error for  $\chi = 16$  in comparison to  $\chi_{\max}$ . (d) From a pure resource perspective, TEBD is favorable over LRK over TDVP and over Krylov when using MPDOs. LPTN-TEBD also scales unfavorably, but the additional link for each site with  $\chi = \kappa$  induces matrices with dimension  $\chi^2$  rather than  $\chi$  affecting the scaling of operations.

$\chi_{\max, \text{MPS}} = \chi_{\max, \text{MPDO}} \kappa_{\max}$ ; in both cases, we split a matrix of  $\chi_{\max, \text{MPS}} d \times \chi_{\max, \text{MPS}} d$ . Thus, we can compare the LPTN data for  $\chi = 16$  with the MPDOs of  $\chi = 256$ . The error does not outweigh the higher CPU time. It remains the question if novel methods for LPTNs can overcome the problem [72], which also consider the optimal ratio between  $\chi$  and  $\kappa$  for LPTNs.

Finally, Figure 6(c) answers in parts how efficiently the different algorithms use their bond dimension. We compare the values of the number operator for MPDOs with  $\chi_{\max} = 1024$  and LPTNs with  $\chi_{\max} = \kappa = 32$  to simulation with lower bond dimension and get a more detailed picture of convergence. MPDOs profit from using a very low bond dimension for TDVP and TEBD. We remark that this model including this initial condition has very low requirements with regards to the bond dimension with MPS and MPDO methods. In fact, simulations with  $\chi_{\max}/64 = 16$  are already not distinguishable from simulations with  $\chi_{\max}$ . In contrast, the LRK method shows, despite the same error in the total number of excitations, an error between bond dimensions 512 and 1024, i.e., they must exceed bond dimensions up to and beyond 512. The Krylov method does not use the full bond dimension according to this data, but is less efficient in using the bond dimension in comparison to TEBD and TDVP. The LPTN algorithm has the highest error for this comparison, although the bond dimension for both links is with 32 much lower. Saturating both links leads to the larger CPU times and the higher error if values are truncated throughout the simulation. The inefficient use of the bond dimension in the LPTN is related to the loop network structure when looking at the complete network representing  $\rho$  instead of its purification. Recent efforts to overcome this problem via intermediate steps have not been considered for this implementation [72].

The quantum trajectories run with  $N_{\text{QT}} = 500$  and yield an error above the MPDO and LPTN result, see again Fig. 6(b). While the error in MPDO and LPTN is solely due to truncation and the error induced by the Trotter decomposition, the QTs could further improve by taking more trajectories. The error follows the law of large numbers. If we consider the CPU times for each method obtained on a *2x(Intel Xeon E5-2680 Dodeca-core) 24 Cores 2.50GHz* node compiled with *ifort*, the QTs exceed with  $N_{\text{QT}} = 500$  already the resources for the MPDO. Here, QTs run with TEBD and, thus, the fastest method. Therefore,

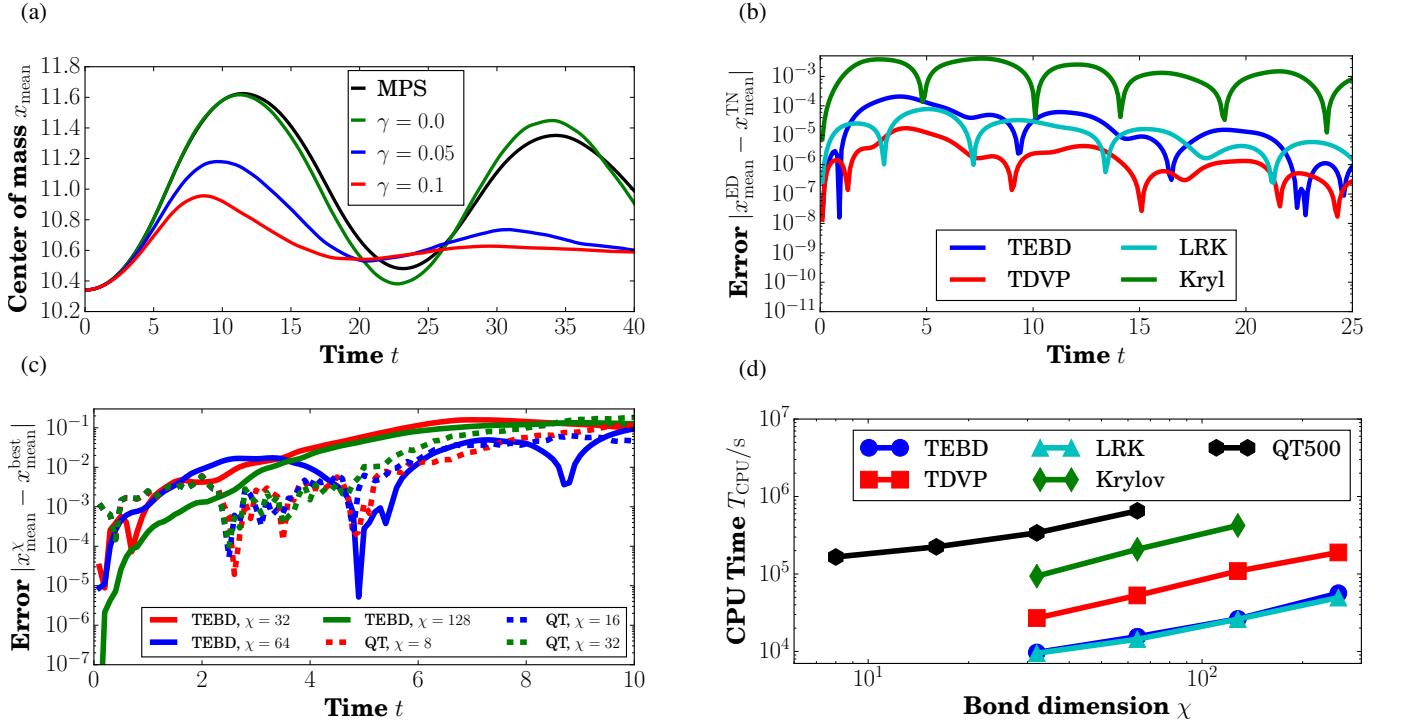


Figure 7. *Convergence of open quantum system Bose-Hubbard dynamics.* (a) The center of mass starts oscillating after we release the potential on the right well at time  $t = 0$  and keep only a one-site potential in the middle to separate wells. We observe that the simulations for MPS and MPDO of a closed system mismatch after about ten time units. The coupling of the system to a dephasing damps the oscillations. (b) We compare the error of tensor network (TN) methods against exact diagonalization for a small system of  $L = 5$ . (c) We compare the errors of QTs with TEBD and  $N_{\text{QT}} = 500$  and simulations with MPDOs and TEBD to the TEBD simulations with the highest bond dimension, i.e.,  $\chi = 256$ . Errors grow fast and show the numerical challenges associated with this problem setup. (d) We compare the computational resources for MPDO and QT algorithms. The coupling to the environment is  $\gamma = 0.05$ . TEBD and LRK use the least resources, then comes TDVP. The quantum trajectories with  $N_{\text{QT}}$  and TEBD are located above MPDOs with TEBD. Due to the limitation in bond dimension in this example and the possibility of parallelizing, they are an attractive option.

more trajectories are not considered as they would increase the difference in CPU time further. This CPU time is the cumulative time for all simulations, and large-scale parallelization can make them favorable for getting a quick picture of the physics. We point out once again the very low bond dimension used in the MPDOs, which makes them favorable, and models with higher entanglement might profit more from QTs. This statement is supported by the next example, i.e., Sec. IV C. We recall that converting an MPS to an MPDO increases the bond dimension from  $\chi$  to  $\chi^2$  and any decomposition, such as an SVD, scales cubically with the matrix dimension.

### C. Local Lindblad operators with symmetry (QT and MPDO)

The last convergence study treats a Lindblad master equation with a conserved quantity. This symmetry restricts us to the usage of QTs and MPDOs. We choose as our Hamiltonian the Bose-Hubbard model

$$H = -J \sum_{k=1}^{L-1} (b_k^\dagger b_{k+1} + h.c.) + \frac{U}{2} \sum_{k=1}^L n_k(n_k - 1) + \sum_{k=1}^L V(k)n_k. \quad (39)$$

$J$  sets the tunneling strength and the repulsive on-site interaction is  $U$ .  $b_k$  ( $b_k^\dagger$ ) is the bosonic annihilation (creation) operator acting on site  $k$ . The Hamiltonian conserves the number of bosons, i.e., the commutator  $[H, N] = 0$  with  $N = \sum_{k=1}^L n_k$ . The chemical potential, i.e.,  $\mu \sum_{k=1}^L n_k$  can be discarded in simulations with number conservation; it represents an energy shift without influence on the simulation. But we include a potential  $V(x)$  to capture the potential of the double well. We choose a dephasing operator as the Lindblad operator, i.e.,  $L_k = n_k$  acting on each site  $k$ .

We consider a double-well scenario with two wells of  $L_W$  sites, separated by a one-site barrier with  $V(L_W + 1) \neq 0$ . The total size of the system is  $L = 2L_W + 1$  and we choose a filling of  $N = L_W$ . The initial state for the time evolution is the

ground state of the particles trapped in the left well with  $V(x) = 1$  ( $V(x) = 0.5$ ) for  $L = 5$  ( $L = 21$ ) for all  $x > L_W$ . At  $t = 0$ , the wave function starts to oscillate between the two wells in a Josephson-like regime. The coupling to the open system damps out the oscillations; we show this effect in Fig. 7(a) with the center of mass, or mean, as a function of time, i.e.,

$$x_{\text{mean}}(t) = \frac{1}{N} \sum_{k=1}^L k n_k(t). \quad (40)$$

Two of the curves show the simulation for closed system time evolution with MPS and MPDO and validate that the MPDO tensor network can simulate the closed system correctly until entanglement generation introduces significant errors to the MPDO. The effects of the dephasing lead to a damping of the oscillation as shown in the two additional curves with  $\gamma = 0.05$  and  $\gamma = 0.1$ . The system size is  $L = 21$ , and we choose an initial bond dimension of the ground state of  $\chi = 5$ . We assume that the ground state has initial errors, but as we compare time evolution methods, all time evolution methods start with the same ground state. As the initial bond dimension of the MPDO is  $\chi^2 = 25$ , that allows us to run with medium bond dimensions and judge on the error due to truncation. The data shown in Fig. 7(a) is for bond dimension  $\chi = 256$  for the MPS and MPDO during the time evolution.

We presented the error for the exciton dynamics based on the exponential decay; we are not aware that we have an equally suited result to compare the dynamics of the double well and Bose-Hubbard model. Thus, we start with a comparison between the tensor network algorithms and exact diagonalization. The OSMPS package includes exact diagonalization methods implemented in Python [73], and one of their purposes is exactly the accessibility for validating other techniques with an independent method. We simulate with  $L = 5$  sites and set the local dimension to  $d = 3$ , i.e., states with more than two bosons per site are truncated. The error of the center of mass for the simulation with TDVP is minimal through most of the simulation and bounded by  $10^{-5}$  according to Fig. 7. The next best methods are LRK and TEBD, while Krylov has the largest error bounded by  $10^{-3}$ . The choice of the position of the center of mass as a macroscopic observable comes with a couple of local minima of the error; the position of the center of mass can align in two states, although the states are different and the envelope is more meaningful and conclusive.

We now analyze how the convergence scales with bond dimension. The trends are similar for the different time evolution methods, where the reason is the exhausted bond dimension and truncation of singular values. Figure 7(c) shows the error in the center of mass of TEBD simulations with bond dimension  $\chi = 32, 64, 128$  to the most accurate simulation with  $\chi = 256$ . The significant difference between the simulations reveals the need for high bond dimensions in this problem and we cut the error plots at ten time units. We conclude that the bond dimension is used completely after very short times for MPDOs; only simulations with  $\chi = 128$  can keep the error below  $10^{-5}$  for the first couple of time steps. The QTs averaged over 500 runs are compared to the most accurate MPDO simulation, both run with TEBD. We have three regimes. (i) The MPDO simulations are more accurate at the very beginning of the time evolution as the QTs suffer from statistical averaging. This regime ends at  $t \approx 2$  (ii) The error of the QTs drops below the MPDO simulations with small bond dimension. The error due to truncation in the MPDO is worse than the error from the average of the trajectories. (iii) For times  $t > 5$ , the difference between the QTs and the MPDO with  $\chi = 256$  grows. Without involving more details, the difference can be due to either method.

Finally, we turn to the actual resources used in Fig. 7(d). We observe that both TEBD and LRK use the same amount of resources. TDVP is less than an order of magnitude above these two methods. The Krylov method takes much longer than TDVP, which is in the end about an order of magnitude difference to the fastest method, i.e., LRK. We run the QTs with a much lower bond dimension; the actual bond dimensions 8 (16) are comparable after squaring it in the transformation from MPS to an MPDO of bond dimension 64 (256). The resources are more than a magnitude higher; we recall that they can be easily parallelized in contrast to an MPDO simulation. The large error at low bond dimension for MPDOs makes QTs much more attractive than in the previous case of the exciton transport.

## V. CONCLUSIONS

In this work, we have presented three different evolution techniques for one-dimensional quantum systems under the Lindblad master equation with tensor network methods. Therefore, the *Open Source Matrix Product States* (OSMPS) package allows the quantum community to explore the advantages of each method. Open quantum system dynamics provide access to more advanced simulations of quantum simulators including the effects of the interaction with the environment as simulated with the Lindblad master equation throughout this work.

We described the bond dimension of the Liouville operator represented as a matrix product operator (MPO); this MPO is used to evolve matrix product density operators beyond nearest-neighbor interactions and the time-evolving block decimation (TEBD), i.e., the time-dependent variational principle, the local Runge-Kutta time evolution, and the Krylov time evolution. Section III A provides insights into the scaling of methods due to the bond dimension of the MPO. For example, non-local rules with a bond dimension  $\chi_{H-MPO}$  to represent the Hamiltonian  $H$  have a bond dimension of  $\chi_{\mathcal{L}-MPO} = 2\chi_{H-MPO}$  to depict the Liouville operator. If we define Lindblad terms analog to Hamiltonian terms, e.g., we replace a nearest-neighbor

interaction of a Hamiltonian with a Lindblad operator acting on nearest-neighbor sites, they have a bond dimension three times as big as  $\chi_{H-MPO}$ . We found that different approaches are favorable in different situations. Locally purified tensor networks (LPTNs) had the best scaling in the example of the finite temperature states of the quantum Ising model. For the dissipative dynamics of an exciton, we found MPDOs as the optimal solution due to the low entanglement throughout the simulation. When the entanglement generated during the time evolution exhausts the maximal bond dimension as observed in the Bose-Hubbard double well, quantum trajectories (QTs) became a good alternative to MPDOs.

The examples also show the problem sizes one can treat with the OSMPS package. The finite temperature states via imaginary time evolution and TEBD can treat almost as many sites as imaginary time evolution with MPS can, i.e., finding the ground state. In detail, we compared the thermal states for  $L = 100$  sites. Changing the local dimension or the final temperature can increase the computational scaling away from the MPS case; the number of time steps necessary scales inversely with the final temperature at a fixed time step in the evolution. CPU times on the order of 1000 seconds on a cluster did not reach the limits of the method.

The exciton dynamics represents an example which does not generate much entanglement during the evolution, and the simulation stays below 100 seconds on an HPC cluster, given the best choice of the method being TEBD with MPDOs. This system is evolved for 30 time units of the local potential with 600 time steps and 80 sites. Bond dimension is not exhausted in the example, where the maximum is set to 512. Admittedly, this system can be scaled up more for research, which was prevented in our case due to the exploration of the methods not scaling favorably.

In contrast, the double well simulation shows the effect of entanglement generated during the time evolution and preventing more precise simulations of larger systems. We have 21 sites with 10 bosons and a local dimension of 4. The MPDO simulations produce visible errors beginning at time 10 in the units of the tunneling at a bond dimension of  $\chi = 256$ . The dissipative Bose-Hubbard model with two-site Lindblad operators using TEBD-MPDO follows the same direction with limited system sizes and further restriction with regards to quantum trajectories and the construction of MPOs.

However, we strongly emphasize that each of the examples presented handles system sizes which are well beyond the means of exact diagonalization and, therefore, tensor networks are a very fruitful possibility to numerically explore these systems in the open quantum dynamics context.

These studies underline the necessity to explore different methods for the simulation of density matrices with tensor networks and choose the most suitable method for pushing the limits in each case. We have presented useful case studies with the quantum Ising model at finite temperature, dissipative exciton dynamics, and the open quantum system Bose-Hubbard modeling a double well with dephasing. Each of them could be a starting point for more extensive studies or serve as a blueprint to study other models, e.g., finite temperature diagrams of other spin models of the *XYZ* class.

Furthermore, the adaption of tensor network methods for open quantum systems beyond one-dimensional cases is another goal for the research community. The adaption of projected entangled pair states, i.e., the two-dimensional analog of a matrix product state, to open quantum systems in [21] has established the foundation for such an approach. These projected entangled pair operators can now be considered for further research applications.

Evidently, tensor network methods have to evolve past the Markovian case of the Lindblad master equation. The development of methods within the tensor network algorithms to capture such non-Markovian effects is one future direction in the design of new methods.

## ACKNOWLEDGMENTS

We gratefully appreciate contributions from and discussions with D. Alcala, I. de Vega, M. T. Lusk, G. Shchedrin, and M. L. Wall. This work has been supported by the AFOSR under grant FA9550-14-1-0287, and the NSF under the grants PHY-1520915 and OAC-1740130. We acknowledge support of the U.K. Engineering and Physical Sciences Research Council (EPSRC) through the “Quantum Science with Ultracold Molecules” Programme (Grant No. EP/P01058X/1). The calculations were carried out using the high performance computing resources provided by the Golden Energy Computing Organization at the Colorado School of Mines. S.M. gratefully acknowledges the support of the DFG via a Heisenberg fellowship and the TWITTER project.

- 
- [1] A. Kossakowski, “On quantum statistical mechanics of non-Hamiltonian systems,” *Reports on Mathematical Physics* **3**, 247 – 274 (1972).
  - [2] G. Lindblad, “On the generators of quantum dynamical semigroups,” *Communications in Mathematical Physics* **48**, 119–130 (1976).
  - [3] Vittorio Gorini, Andrzej Kossakowski, and E. C. G. Sudarshan, “Completely positive dynamical semigroups of N-level systems,” *Journal of Mathematical Physics* **17**, 821–825 (1976).
  - [4] Heinz-Peter Breuer and Francesco Petruccione, *The Theory of Open Quantum Systems*, 1st ed. (Clarendon Press, Oxford, 2009).
  - [5] Attal Stéphane, Alain Joye, and Claude-Alain Pillet, *Open Quantum Systems II: The Markovian Approach* (Springer, 2006).
  - [6] Angel Rivas and Susana F Huelga, *Open Quantum Systems* (Springer, Heidelberg Dordrecht London New York, 2012).

- [7] Gernot Schaller, *Open quantum systems far from equilibrium*, Vol. 881 (Springer, 2004).
- [8] Yoshitaka Tanimura and Ryogo Kubo, “Time Evolution of a Quantum System in Contact with a Nearly Gaussian-Markoffian Noise Bath,” *Journal of the Physical Society of Japan* **58**, 101–114 (1989).
- [9] Yoshitaka Tanimura, “Nonperturbative expansion method for a quantum system coupled to a harmonic-oscillator bath,” *Phys. Rev. A* **41**, 6676–6687 (1990).
- [10] Inés de Vega and Daniel Alonso, “Dynamics of non-Markovian open quantum systems,” *Rev. Mod. Phys.* **89**, 015001 (2017).
- [11] Steven R. White, “Density matrix formulation for quantum renormalization groups,” *Phys. Rev. Lett.* **69**, 2863–2866 (1992).
- [12] Steven R. White, “Density-matrix algorithms for quantum renormalization groups,” *Phys. Rev. B* **48**, 10345–10356 (1993).
- [13] U. Schollwöck, “The density-matrix renormalization group,” *Rev. Mod. Phys.* **77**, 259–315 (2005).
- [14] Guifré Vidal, “Efficient Classical Simulation of Slightly Entangled Quantum Computations,” *Phys. Rev. Lett.* **91**, 147902 (2003).
- [15] Ulrich Schollwöck, “The density-matrix renormalization group in the age of matrix product states,” *Annals of Physics* **326**, 96 – 192 (2011), January 2011 Special Issue.
- [16] Román Orús, “A practical introduction to tensor networks: Matrix product states and projected entangled pair states,” *Annals of Physics* **349**, 117 – 158 (2014).
- [17] G. Kin-Lic Chan, A. Keselman, N. Nakatani, Z. Li, and S. R. White, “Matrix Product Operators, Matrix Product States, and ab initio Density Matrix Renormalization Group algorithms,” *ArXiv e-prints* 1605.02611 (2016).
- [18] Y.-Y. Shi, L.-M. Duan, and G. Vidal, “Classical simulation of quantum many-body systems with a tree tensor network,” *Phys. Rev. A* **74**, 022320 (2006).
- [19] G. Vidal, “Class of Quantum Many-Body States That Can Be Efficiently Simulated,” *Phys. Rev. Lett.* **101**, 110501 (2008).
- [20] F. Verstraete, V. Murg, and J.I. Cirac, “Matrix product states, projected entangled pair states, and variational renormalization group methods for quantum spin systems,” *Advances in Physics* **57**, 143–224 (2008).
- [21] Augustine Kshetrimayum, Hendrik Weimer, and Román Orús, “A simple tensor network algorithm for two-dimensional steady states,” *Nature Communications* **8**, 1291 (2017).
- [22] J. Eisert, M. Cramer, and M. B. Plenio, “*Colloquium* : Area laws for the entanglement entropy,” *Rev. Mod. Phys.* **82**, 277–306 (2010).
- [23] Hendrik Weimer, “Variational principle for steady states of dissipative quantum many-body systems,” *Phys. Rev. Lett.* **114**, 040402 (2015).
- [24] Jian Cui, J. Ignacio Cirac, and Mari Carmen Bañuls, “Variational matrix product operators for the steady state of dissipative quantum systems,” *Phys. Rev. Lett.* **114**, 220601 (2015).
- [25] Eduardo Mascarenhas, Hugo Flayac, and Vincenzo Savona, “Matrix-product-operator approach to the nonequilibrium steady state of driven-dissipative quantum arrays,” *Phys. Rev. A* **92**, 022116 (2015).
- [26] Jean Dalibard, Yvan Castin, and Klaus Mølmer, “Wave-function approach to dissipative processes in quantum optics,” *Phys. Rev. Lett.* **68**, 580–583 (1992).
- [27] R. Dum, P. Zoller, and H. Ritsch, “Monte Carlo simulation of the atomic master equation for spontaneous emission,” *Phys. Rev. A* **45**, 4879–4887 (1992).
- [28] H. M. Wiseman, “Quantum trajectories and quantum measurement theory,” *Quantum and Semiclassical Optics: Journal of the European Optical Society Part B* **8**, 205 (1996).
- [29] M. B. Plenio and P. L. Knight, “The quantum-jump approach to dissipative dynamics in quantum optics,” *Rev. Mod. Phys.* **70**, 101–144 (1998).
- [30] Howard Carmichael, *An open systems approach to quantum optics: lectures presented at the Université Libre de Bruxelles, October 28 to November 4, 1991*, Vol. 18 (Springer Science & Business Media, 2009).
- [31] F. Verstraete, J. García-Ripoll, and J. Cirac, “Matrix Product Density Operators: Simulation of Finite-Temperature and Dissipative Systems,” *Phys. Rev. Lett.* **93**, 207204 (2004).
- [32] Michael Zwolak and Guifré Vidal, “Mixed-State Dynamics in One-Dimensional Quantum Lattice Systems: A Time-Dependent Super-operator Renormalization Algorithm,” *Phys. Rev. Lett.* **93**, 207205 (2004).
- [33] A. H. Werner, D. Jaschke, P. Silvi, M. Kliesch, T. Calarco, J. Eisert, and S. Montangero, “Positive Tensor Network Approach for Simulating Open Quantum Many-Body Systems,” *Phys. Rev. Lett.* **116**, 237201 (2016).
- [34] E. M. Stoudenmire and Steven R. White, “Minimally entangled typical thermal state algorithms,” *New Journal of Physics* **12**, 055026 (2010).
- [35] Gemma De las Cuevas, Norbert Schuch, David Pérez-García, and J Ignacio Cirac, “Purifications of multipartite states: limitations and constructive methods,” *New Journal of Physics* **15**, 123021 (2013).
- [36] M. Kliesch, D. Gross, and J. Eisert, “Matrix-Product Operators and States: NP-Hardness and Undecidability,” *Phys. Rev. Lett.* **113**, 160503 (2014).
- [37] Gemma De las Cuevas, T. S. Cubitt, J. I. Cirac, M. M. Wolf, and David Pérez-García, “Fundamental limitations in the purifications of tensor networks,” *Journal of Mathematical Physics* **57**, 071902 (2016).
- [38] L. Bonnes and A. M. Läuchli, “Superoperators vs. Trajectories for Matrix Product State Simulations of Open Quantum System: A Case Study,” *ArXiv e-prints* 1411.4831 (2014).
- [39] Hendrik Weimer, Markus Müller, Igor Lesanovsky, Peter Zoller, and Hans Peter Büchler, “A Rydberg quantum simulator,” *Nature Physics* **6**, 382 (2010).
- [40] Yiwen Chu, Prashanta Kharel, William H. Renninger, Luke D. Burkhardt, Luigi Frunzio, Peter T. Rakich, and Robert J. Schoelkopf, “Quantum acoustics with superconducting qubits,” *Science* **358**, 199–202 (2017).
- [41] Yiwen Chu, Prashanta Kharel, William H. Renninger, Luke D. Burkhardt, Luigi Frunzio, Peter T. Rakich, and Robert J. Schoelkopf, Supplemental material of [40].
- [42] Julio T. Barreiro, Markus Müller, Philipp Schindler, Daniel Nigg, Thomas Monz, Michael Chwalla, Markus Hennrich, Christian F. Roos, Peter Zoller, and Rainer Blatt, “An open-system quantum simulator with trapped ions,” *Nature* **470**, 486 – 491 (2011).

- [43] P. Schindler, M. Müller, D. Nigg, J. T. Barreiro, E. A. Martinez, M. Hennrich, T. Monz, S. Diehl, P. Zoller, and R. Blatt, “Quantum simulation of dynamical maps with trapped ions,” *Nature Physics* **9**, 361 EP – (2013), article.
- [44] Paola Cappellaro, “Lecture notes “22.51 Quantum Theory of Radiation Interactions, Fall 2012”,,” (2012).
- [45] Markus Müller, Sebastian Diehl, Guido Pupillo, and Peter Zoller, “Engineered Open Systems and Quantum Simulations with Atoms and Ions,” in *Advances in Atomic, Molecular, and Optical Physics*, Advances In Atomic, Molecular, and Optical Physics, Vol. 61, edited by Paul Berman, Ennio Arimondo, and Chun Lin (Academic Press, 2012) pp. 1 – 80.
- [46] Hannes Pichler, Johannes Schachenmayer, Andrew J. Daley, and Peter Zoller, “Heating dynamics of bosonic atoms in a noisy optical lattice,” *Phys. Rev. A* **87**, 033606 (2013).
- [47] Lincoln D. Carr, David DeMille, Roman V. Krems, and Jun Ye, “Cold and ultracold molecules: science, technology and applications,” *New Journal of Physics* **11**, 055049 (2009).
- [48] Matthijs P. Branderhorst, Pablo Londero, Piotr Wasylczyk, Ian Walmsley, Constantin Brif, Herschel Rabitz, and Robert Kosut, “Coherent Control of Decoherence in Diatomic Molecules,” in *Conference on Lasers and Electro-Optics/Quantum Electronics and Laser Science Conference and Photonic Applications Systems Technologies* (Optical Society of America, 2006) p. JTuB2.
- [49] Daniel Jaschke, Michael L. Wall, and Lincoln D. Carr, “Open source Matrix Product States: Opening ways to simulate entangled many-body quantum systems in one dimension,” *Computer Physics Communications* **225**, 59–91 (2018).
- [50] R Biele and R D’Agosta, “A stochastic approach to open quantum systems,” *Journal of Physics: Condensed Matter* **24**, 273201 (2012).
- [51] Man-Duen Choi, “Completely positive linear maps on complex matrices,” *Linear Algebra and its Applications* **10**, 285 – 290 (1975).
- [52] Andrew J. Daley, “Quantum trajectories and open many-body quantum systems,” *Advances in Physics* **63**, 77–149 (2014).
- [53] B Pirvu, V Murg, J I Cirac, and F Verstraete, “Matrix product operator representations,” *New Journal of Physics* **12**, 025012 (2010).
- [54] M. L. Wall and Lincoln D. Carr, “Out-of-equilibrium dynamics with matrix product states,” *New Journal of Physics* **14**, 125015 (2012).
- [55] Michael P. Zaletel, Roger S. K. Mong, Christoph Karrasch, Joel E. Moore, and Frank Pollmann, “Time-evolving a matrix product state with long-ranged interactions,” *Phys. Rev. B* **91**, 165112 (2015).
- [56] Jutho Haegeman, Christian Lubich, Ivan Oseledets, Bart Vandereycken, and Frank Verstraete, “Unifying time evolution and optimization with matrix product states,” *Phys. Rev. B* **94**, 165116 (2016).
- [57] Cleve Moler and Charles Van Loan, “Nineteen Dubious Ways to Compute the Exponential of a Matrix, Twenty-Five Years Later,” *SIAM Review* **45**, 3–49 (2003).
- [58] Peter Schmitteckert, “Nonequilibrium electron transport using the density matrix renormalization group method,” *Phys. Rev. B* **70**, 121302 (2004).
- [59] Juan José García-Ripoll, “Time evolution of matrix product states,” *New Journal of Physics* **8**, 305 (2006).
- [60] E. Gallopoulos and Y. Saad, “Efficient Solution of Parabolic Equations by Krylov Approximation Methods,” *SIAM Journal on Scientific and Statistical Computing* **13**, 1236–1264 (1992).
- [61] Y. Saad, “Analysis of Some Krylov Subspace Approximations to the Matrix Exponential Operator,” *SIAM Journal on Numerical Analysis* **29**, 209–228 (1992).
- [62] Jutho Haegeman, J. Ignacio Cirac, Tobias J. Osborne, Iztok Pižorn, Henri Verschelde, and Frank Verstraete, “Time-dependent variational principle for quantum lattices,” *Phys. Rev. Lett.* **107**, 070601 (2011).
- [63] Vincent R. Overbeck and Hendrik Weimer, “Time evolution of open quantum many-body systems,” *Phys. Rev. A* **93**, 012106 (2016).
- [64] Michael A. Nielsen and Isaac L. Chuang, *Quantum Computation and Quantum Information*, 9th ed. (Cambridge Univ. Press, Cambridge, United Kingdom, 2007).
- [65] A. T. Sornborger and E. D. Stewart, “Higher-order methods for simulations on quantum computers,” *Phys. Rev. A* **60**, 1956–1965 (1999).
- [66] A. Osterloh, Luigi Amico, G. Falci, and Rosario Fazio, “Scaling of entanglement close to a quantum phase transition,” *Nature* **416**, 608 (2002).
- [67] G. Vidal, J. I. Latorre, E. Rico, and A. Kitaev, “Entanglement in quantum critical phenomena,” *Phys. Rev. Lett.* **90**, 227902 (2003).
- [68] T. Prosen, “Exact Nonequilibrium Steady State of a Strongly Driven Open  $XXZ$  Chain,” *Phys. Rev. Lett.* **107**, 137201 (2011).
- [69] Mark T. Lusk, Charles A. Stafford, Jeremy D. Zimmerman, and Lincoln D. Carr, “Control of exciton transport using quantum interference,” *Phys. Rev. B* **92**, 241112 (2015).
- [70] Xiaoning Zang, Simone Montangero, Lincoln D. Carr, and Mark T. Lusk, “Engineering and manipulating exciton wave packets,” *Phys. Rev. B* **95**, 195423 (2017).
- [71] M B Plenio and S F Huelga, “Dephasing-assisted transport: quantum networks and biomolecules,” *New Journal of Physics* **10**, 113019 (2008).
- [72] Hannes Wegener and Simone Montangero, In prep.
- [73] D. Jaschke and L. D. Carr, “Open source Matrix Product States: Exact diagonalization and other entanglement-accurate methods revisited in quantum systems,” *ArXiv e-prints* 1802.10052 (2018).
- [74] S. Diehl, A. Micheli, A. Kantian, B. Kraus, H. P. Büchler, and P. Zoller, “Quantum states and phases in driven open quantum systems with cold atoms,” *Nature Physics* **4**, 878 – 883 (2008).
- [75] B. Kraus, H. P. Büchler, S. Diehl, A. Kantian, A. Micheli, and P. Zoller, “Preparation of entangled states by quantum Markov processes,” *Phys. Rev. A* **78**, 042307 (2008).
- [76] G. Kordas, D. Witthaut, P. Buonsante, A. Vezzani, R. Burioni, A. I. Karanikas, and S. Wimberger, “The dissipative Bose-Hubbard model,” *The European Physical Journal Special Topics* **224**, 2127–2171 (2015).
- [77] S. Ejima, H. Fehske, and F. Gebhard, “Dynamic properties of the one-dimensional Bose-Hubbard model,” *EPL (Europhysics Letters)* **93**, 30002 (2011).

### Appendix A: Non-Local Lindblad operators with symmetry (MPDO)

We discuss the case of a non-local Lindblad operator acting on two neighboring sites and explain the challenges such equations face. The Lindblad operators conserve the number of bosons. We choose as a Hamiltonian the Bose-Hubbard model, but in contrast to Eq. (A1) we do not have an on-site potential,

$$H = -J \sum_{k=1}^{L-1} (b_k^\dagger b_{k+1} + h.c.) + \frac{U}{2} \sum_{k=1}^L n_k (n_k - 1). \quad (\text{A1})$$

$J$  sets the tunneling strength and the repulsive on-site interaction is  $U$ .  $b_k$  ( $b_k^\dagger$ ) is the bosonic annihilation (creation) operator acting on site  $k$ . The Hamiltonian conserves the number of bosons, i.e., the commutator  $[H, N] = 0$  with  $N = \sum_{k=1}^L n_k$ . The chemical potential, i.e.,  $\mu \sum_{k=1}^L n_k$  can be discarded in simulations with number conservation; it represents an energy shift without influence on the simulation. The dissipative state preparation for the Bose-Hubbard model is the focus of the references [74, 75] and further discussed in [45, 76]. We use the Lindblad operators from these approaches, i.e.,

$$L_k = (b_k^\dagger + b_{k+1}^\dagger) (b_k - b_{k+1}), \quad k \in \{1, \dots, (L-1)\}. \quad (\text{A2})$$

This formulation is not directly suitable for any of our Lindblad rule sets. In fact, the two-site operator is not a product term and is therefore challenging. We recall that a Lindblad operator of the type  $L = A + B$  cannot be split into two Lindblad operators  $L_A = A$  and  $L_B = B$ ; a look at the corresponding terms of  $L\rho L^\dagger$  reveals the missing cross-terms. Thus, we create a new type of rule set which is similar to the many-body string Lindblad operators, but allows us to define different operators for the operators on the left and right:

$$L_{A,k \dots k'} \rho L_{B,k \dots k'}^\dagger - \frac{1}{2} \left\{ L_{B,k \dots k'}^\dagger L_{A,k \dots k'}, \rho \right\}, \quad (\text{A3})$$

$$L_{A,k \dots k'} = L_{A,k} \otimes L_{A,k+1} \otimes \dots \otimes L_{A,k'}, \quad (\text{A4})$$

$$L_{B,k \dots k'} = L_{B,k} \otimes L_{B,k+1} \otimes \dots \otimes L_{B,k'}. \quad (\text{A5})$$

Now, we can define the following set of Lindblad operators  $L_\mu$

$$\begin{aligned} L_{\mu=1,k} &= n_k; \quad L_{\mu=2,A,k} = n_k, L_{\mu=2,B,k} = -b_k^\dagger b_{k+1}; \\ L_{\mu=3,A,k} &= n_k, L_{\mu=3,B,k} = b_k b_{k+1}^\dagger; \quad L_{\mu=4,A,k} = n_k, L_{\mu=4,B,k} = -n_{k+1}; \\ L_{\mu=5,A,k} &= -b_k^\dagger b_{k+1}, L_{\mu=5,B,k} = n_k; \quad L_{\mu=6,A,k} = -b_k^\dagger b_{k+1}, L_{\mu=6,B,k} = -b_k^\dagger b_{k+1}; \\ L_{\mu=7,A,k} &= -b_k^\dagger b_{k+1}, L_{\mu=7,B,k} = b_k b_{k+1}^\dagger; \quad L_{\mu=8,A,k} = -b_k^\dagger b_{k+1}, L_{\mu=8,B,k} = -n_{k+1}; \\ L_{\mu=9,A,k} &= b_k b_{k+1}^\dagger, L_{\mu=9,B,k} = n_k; \quad L_{\mu=10,A,k} = b_k b_{k+1}^\dagger, L_{\mu=10,B,k} = -b_k^\dagger b_{k+1}; \\ L_{\mu=11,A,k} &= b_k b_{k+1}^\dagger, L_{\mu=11,B,k} = b_k b_{k+1}^\dagger; \quad L_{\mu=12,A,k} = b_k b_{k+1}^\dagger, L_{\mu=12,B,k} = -n_{k+1}; \\ L_{\mu=13,A,k} &= n_{k+1}, L_{\mu=13,B,k} = n_k; \quad L_{\mu=14,A,k} = n_{k+1}, L_{\mu=14,B,k} = -b_k^\dagger b_{k+1}; \\ L_{\mu=15,A,k} &= n_{k+1}, L_{\mu=15,B,k} = b_k b_{k+1}^\dagger; \quad L_{\mu=16,k} = n_{k+1}. \end{aligned} \quad (\text{A6})$$

The representation of this set of Lindblad operators together with the Hamiltonian in an MPO is not recommended. We have a bond dimension of 48 (2 for local terms, 4 for tunneling in the Hamiltonian,  $3 \times 14$  for the nearest-neighbor Lindblad terms). From the perspective of this bond dimension, only TEBD remains as a valid option for time evolution with MPDOs. QTs have problems due to the different terms  $L_{A,k \dots k'}$  and  $L_{B,k \dots k'}$ . Therefore, extension of the QTs to Lindblad operators with no convenient representation in terms of rule sets, such as the example in Eq. (A2), are convenient and considered for the future.

The coupling of the single-site Lindblad operator  $n_k$  is a function of the lattice site; the two boundary sites have only half the coupling of the bulk. We point out that each of the terms conserves the number of bosons in the system and thus the Liouville operator commutes with the global number operator  $N$ , i.e.,  $[\mathcal{L}, N \otimes \mathbb{I} + \mathbb{I} \otimes N^T] = 0$ . We defined this condition in Eq. (7).

For the simulation, we start in the ground state of the Bose-Hubbard model in the Mott insulating phase at unit filling. The BKT transition is around  $J/U \approx 0.305$  [77] in the thermodynamic limit. We choose  $J = 0.1$  and  $U = 1.0$  is the energy scale. At  $t = 0$ , we couple the system to the reservoir with the Lindblad operators defined in Eq. (A3). We define the depletion as  $\xi = 1 - \max_i (\Xi_i) / \sum_i \Xi_i$  with  $\Xi_i$  being the eigenvalues of the single-particle density matrix  $\langle b_k^\dagger b_{k'} \rangle$ . The depletion decreases for the superfluid as compared to the Mott insulator when dealing with ground states.

Figure 8(a) describes the evolution of the depletion towards the steady state. We choose a system size of  $L = 20$  and consider states up to two bosons; we have a local dimension of  $d = 3$ . The data is for a bond dimension of  $\chi = 256$ . The steady state differs for the coupling strengths  $\gamma = 0.01, 0.05, 0.1$  and has a lower depletion for stronger coupling to the reservoir. We now

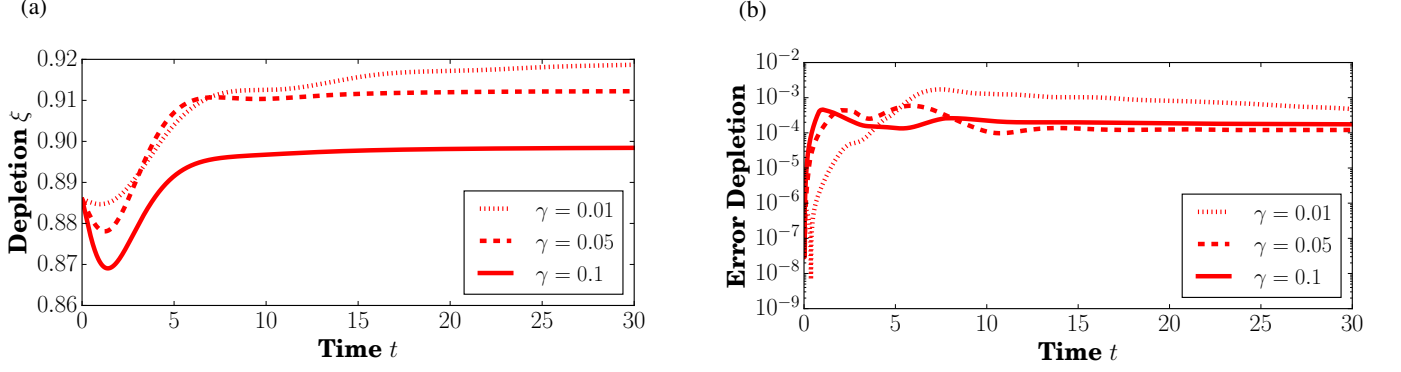


Figure 8. *Non-local Lindblads with the Bose-Hubbard model.* (a) The dynamics of the depletion converging to the steady-state value with a two-site nearest-neighbor Lindblad operator. (b) We calculate the dynamics for a small system  $L = 5$  with exact diagonalization and TEBD and show the error of the TEBD as compared to exact diagonalization for the depletion with three different coupling strenghts  $\gamma$ .

look at the convergence of the different methods; unfortunately, we are not aware of a good observable to check as we had with the exponential decay in the exciton example. Thus, we compare between the exact diagonalization implementation and the tensor network algorithms in Fig. 8(b). We consider a system size of  $L = 5$  due to the restriction of simulation a system in Liouville space with exact diagonalization methods. We obtain that the value of the depletion is converged at the order of  $10^{-3}$  where the value of the depletion is on the order of one. The bond dimension for the MPDO simulation is  $\chi = 100$ .

We conclude that the simulation of Lindblad operators acting on multiple sites is possible. For such operators which cannot be represented as product term, the simulation can get expensive to infeasible when MPOs and the corresponding time evolution method are used. The TEBD algorithm, as shown in this example, is the most convenient alternative for such system dealing only with nearest-neighbor interactions. We recall that TEBD is restricted to nearest-neighbor terms in OSMPS.

### Appendix B: Bond dimension infinite-T Bose-Hubbard state

We derive an upper bound for the bond dimension of the Bose-Hubbard model in an MPDO for the infinite temperature states. We assume that we have a local dimension  $d$  and a filling of  $N$  particles. We pick  $L$  sufficiently large such that  $d \ll L$  and  $N \approx L$ . We pick a site in the middle of the system and obtain  $N + 1$  blocks in the block-diagonal structure. The first  $d$  blocks have bond dimensions  $1, 2, \dots, d$  and the last  $d$  blocks have bond dimensions  $d, d - 1, \dots, 2, 1$ . The remaining fillings have a bond dimension of  $d$ . Thus, we have a total number of subtensors

$$n = d(N - 2d + 1) + d(d + 1) = d(N - d + 2), \quad (\text{B1})$$

where the number of subtensors can serve as an upper bound to estimate the bond dimension  $\chi$ , i.e.,  $\chi \leq n$ .